Rishi Suman

Finite Set Model Predictive Current Control of a Grid Converter Equipped with an LCL Filter

School of Electrical Engineering

Thesis submitted for examination for the degree of Master of Science in Technology.

Espoo 10.03.2017

Thesis supervisor:

Prof. Marko Hinkkanen

Thesis advisor:

Zhanfeng Song, D.Sc. (Tech.)

Aalto University
School of Electrical
Engineering

AALTO UNIVERSITY
SCHOOL OF ELECTRICAL ENGINEERING

ABSTRACT OF THE
MASTER'S THESIS

Author: Rishi Suman

Title: Finite Set Model Predictive Current Control of a Grid Converter Equipped with an LCL Filter

Date: 10.03.2017 Language: English Number of pages:8+51

Department of Electrical Engineering

Professorship: Electrical Drives Code: S-3016

Supervisor: Prof. Marko Hinkkanen

Advisor: Zhanfeng Song, D.Sc. (Tech.)

A grid converter is a critical component used to synchronize a renewable energy source with the utility grid and are also used as an active front-end rectifier for motor drives. Converter switching actions produce harmonics and therefore, it is equipped with an LCL filter to feed smooth sinusoidal current to the grid. However, the resonance behaviour of LCL filter amplifies the harmonics appearing at its resonant frequencies, therefore resonance damping is necessary. This thesis proposes a current controller based upon finite set model predictive control for current tracking and active damping of the LCL filter resonance. The current prediction for the controller is done in a small horizon window and the possibility to extend it to longer horizon has been explored. A hold equivalent discrete-time model with zero-order-hold assumption is used by the controller for predicting current for future time instants using the present state measurement. The current controller also uses an observer to enhance its disturbance rejection capability and reduce the need of additional sensors required to run the controller. The dynamic performance and robustness of the finite set model predictive current controller is demonstrated through simulation results.

Keywords: Current controller, disturbance rejection, finite set, LCL filter, observer, model predictive control, resonance damping

Preface

This thesis work was carried out at Aalto University, Finland in the department of Electrical Engineering and Automation between September 2016 and February 2017. I would like to express my deepest gratitude to my supervisor Prof. Marko Hinkkanen for giving me this wonderful opportunity to work on this research topic. I would like to thank him for his guidance, valuable suggestions and useful corrections in scientific writing. This thesis work cannot be completed without the regular guidance from my instructor Dr. Zhanfeng Song who was providing an active support in doing simulation.

Many useful discussions with Asad, Jussi, Jarno, Seppo and other colleagues from electric drives group helped me to move forward in this challenging journey and provided a nice working environment. I would also like to express my gratitude to Mr. Ari Havisto for arranging all the technical resources required for this thesis.

Finally, I would like to thank my parents and other family members for giving moral support during these months. I also express my gratitude to Abdul, Ahmad and friends at Aalto University for making the stay enjoyable.

Espoo, 10.03.2017

Rishi Suman

Contents

Symbols and Abbreviations

Symbols

Boldface letters represent the matrices, vectors and complex-valued variables. Stationary-reference-frame vectors and matrices are marked with the superscript s. Estimated variables are marked with hat. Estimation-error quantities are marked with a tilde. Reference values are marked with the subscript ref.

$\mathbf{A}, \mathbf{B}_\mathrm{c}, \mathbf{B}_\mathrm{g}, \mathbf{C}_\mathrm{c}$	matrices of state-space representation
C_{dc}	DC-link capacitance
C_f	LCL-filter capacitance
g	cost function
$\boldsymbol{i}_\mathrm{c}$	converter current vector
$i_\mathrm{ca}, i_\mathrm{cb}, i_\mathrm{cc}$	converter phase currents
$\boldsymbol{i}_\mathrm{c}^\mathrm{p}$	predicted converter current
$\boldsymbol{i}_\mathrm{c,ref}$	converter current reference
$\boldsymbol{i}_\mathrm{c,VR}$	virtual converter current
i_{cd}, i_{cq}	real and imaginary component of $\boldsymbol{i}_\mathrm{c}$
$\boldsymbol{i}_\mathrm{g}$	grid current vector
i_{ga}, i_{gb}, i_{cc}	grid phase currents
i_dc	DC current
$\mathbf{I}$	3×3 identity matrix
j	imaginary unit
J	cost function in terms of optimal control
k	discrete-time index
$\mathbf{K_o}$	observer gain vector
k_{o1}, k_{o2}, k_{o3}	elements of the observer gain vector
L_{fc}	converter side inductance of LCL filter
L_{fg}	grid side inductance of LCL filter
$L_t = L_{fc} + L_{fg}$	total inductance
p_c	active power of converter
p_g	active power at the PCC

q_c	reactive power of converter
q_g	reactive power at the PCC
R_d	resistance of passive damping resistor
R_v	resistance of virtual damping resistor
s	Laplace variable
$\mathbf{S}$	switching state vector
$S_\mathrm{a}, S_\mathrm{b}, S_\mathrm{c}$	switching state of individual converter legs
t	time
T_s	sampling time
$\boldsymbol{u}_\mathrm{c}$	convrter voltage vector
$u_\mathrm{a}, u_\mathrm{b}, u_\mathrm{c}$	converter phase voltages
u_dc	DC-link voltage
$\boldsymbol{u}_\mathrm{f}$	LCL-filter capacitor voltage vector
$\boldsymbol{u}_\mathrm{g}$	grid voltage vector
u_g	magnitude of grid voltage vector
$u_\mathrm{ga}, u_\mathrm{gb}, u_\mathrm{gc}$	grid phase voltages
$\mathbf{U}_\mathrm{c,unc}$	unconstrained converter voltage vector
$\mathbf{U}_\mathrm{c}$	converter voltage vector for optimal control
$\mathbf{U}_\mathrm{g}$	grid voltage vector for optimal control
w	disturbance
$\mathbf{x}$	state vector
$\gamma = e^{-j\omega_g T_s}$	complex auxiliary variable
$\boldsymbol{\Gamma}_\mathrm{c}, \boldsymbol{\Gamma}_\mathrm{g}$	input vectors
$\boldsymbol{\Gamma}$	input matrix for optimal control
$\boldsymbol{\Psi}$	input matrix for optimal control
$\boldsymbol{\Upsilon}$	input matrix for optimal control
θ_g	grid voltage angle
$\boldsymbol{\Phi}$	system matrix
ω_g	angular frequency of grid voltage
ω_p	angular resonance frequency of an LCL filter
ω_z	angular anti-resonance frequency of an LCL filter

Abbreviations

AC	alternating current
CS	continuous set
DC	direct current
FS	finite set
LCL	inductor-capacitor-inductor (filter)
MPC	model predictive control
PCC	point of common coupling
PI	proportional integral
PLL	phase-locked loop
PWM	pulse-width modulation
SVPWM	space-vector pulse-width modulation
THD	total harmonic distortion
VSC	voltage source converter
ZOH	zero-order hold

1 Introduction

1.1 Background and motivation

The energy resources which can be replenished naturally over a human time scale are termed as renewable energy sources, such as sunlight, wind, tides, rain, wood and geothermal heat. The world has seen a massive increase in the production of renewable energy during the last decade due to its contribution towards curbing carbon emission, which is considered as the major cause of global climate change. The connection of renewal energy sources to the utility grid requires a dc/ac conversion stage, which is accomplished by a grid converter. Therefore, grid converters play a crucial role in interfacing renewable energy sources to the utility grid and improve stability and power quality at the same time [1].

Grid converters are used to transfer power from DC power sources by injecting sinusoidal current into the grid. They are also increasingly used as active front-end rectifier for motor drives. In doing so, the grid converters generate harmonics, which are harmful for the sensitive equipment connected to the grid. In order to meet the grid-code requirement of providing cleaner input current (with less total harmonic distortion), it is crucial to introduce a filter (L or LCL filter) between the grid converter and the point of common coupling (PCC) of the grid [2]. Interfacing the grid with converters via LCL filters has increased in the past few years. It provides better current quality at low cost and small size in comparison with the conventional L filter [1]. However, using LCL filter has a disadvantage of LCL resonance. The resonant behavior of the LCL filter amplifies the harmonic component close to the resonant frequency, thus deteriorating the quality of the grid current [3]. The resonant behavior can be actively damped using a virtual resistance or can be passively damped at the expense of power losses [2, 4].

Various methods are available for the control of power converters, such as hysteresis control, linear control and predictive control. The most common choice used for grid converters is based on voltage oriented control using a proportional integral (PI) controller. The semiconductors in the converter operate either in the saturation region or in the cut-off region, behaving as an electronic switch. This makes

the converter system non-linear [5]. Model predictive control can include the system constraints, non-linearities and other technical requirements directly into the cost function of the controller.

Model predictive control (MPC) uses a system model for calculating predictions of the future behavior of the controlled variables and then uses an optimization criterion to solve the control objectives for selecting the proper actuation. Calculating predictions and solving the control objective is a tedious calculation burden and the slow processing power of the early microprocessors limited the use of MPC in grid converters. However, the development in the semiconductor technology has increased the computation capabilities of the digital microprocessors required for control purpose [5, 7].

MPC for grid converters can be broadly classified into two main methods, continuous set MPC (CS-MPC) and finite set MPC (FS-MPC). CS-MPC uses continuous time signals as control actions sent to a modulator. Therefore, CS-MPC has a fixed switching frequency. The optimization problem is solved analytically for unconstrained case and a quadratic cost function is solved for a constrained case [8]. Grid converters have limited numbers of switching states and FS-MPC uses these switching states to solve the optimization problem and generate control action only for those switching states. This makes the possible control actions finite. The focus of this study will be on FS-MPC.

The current controller designed using FS-MPC uses the present time instant value of converter current to perform optimization and generate a voltage, having variable switching frequency and a spectrum spread over a wide range of frequency. The voltage spectrum can be modified to resemble the voltage spectrum of pulse width modulation [9]. The variable switching frequency can be used as an advantage to produce low average switching frequecy. Low average switching frequecy will produce low switching loses. Thus, very low switching frequency can be achieved using FS-MPC; which is very important for medium and high voltage application [10].

1.2 Objectives

The objective of this thesis is to design a FS model predictive current controller for a grid converter using an exact discrete-time model and damp the LCL filter resonance using active damping. Emphasis is also to be laid upon designing an observer to reduce sensor and enhance the disturbance (parameter variation) rejection capability of the system. Further, the effect of increasing the horizon on the performance and computation time has to be analyzed. The performance of the FS model predictive current controller is to be compared with the performance of an observer based state space current controller.

1.3 Thesis structure

The thesis comprises of 7 chapters. Chapter 2 explains the continuous and discrete time model of an LCL filter. It also introduces the grid converter model and explains the coordinate transformation of the converter voltage. Chapter 3 introduces the implementation of FS model predictive current controller using a two-level grid converter. It gives a detailed explanation about the usage of discrete model and finite switching state of the converter to track the current reference by optimizing the cost function. It also explains about optimal control and cost function modification to reduce switching frequency. Chapter 4 explains the resonant behavior of LCL filters and the method adopted to damp the resonance. Chapters 5 explains the implementation of state observer to reduce the number of sensors and enhance the disturbance rejection capability of the controller. Chapter 6 gives the simulation results and analyzes the performance in comparison with an observer based state-space controller. The thesis is concluded in Chapter 7 based upon the results drawn from the previous chapter.

2 Grid converter with an LCL filter

Model predictive control (MPC) utilizes a system model for making prediction. Therefore, a proper system model and discretization of the model is important to design a predictive controller that can accurately predict the system output for future time instants. This chapter explains the continuous-time model and zero-order-hold discrete-time model of a two-level grid connected voltage source converter (VSC) equipped with an LCL filter.

2.1 Grid converter model

A typical change-over switch model of a three-phase two-level VSC having 8 switching states is shown in Fig. 2.1. Each change-over switch (a, b and c) can be realized by a pair of insulated gate bipolar transistor with a free-wheeling diode connected in anti-parallel. These pairs are switched *on* and *off* by complimentary signals allowing continuous bi-directional flow of power and current. If both the switches in a pair are in *on* state, then it will lead to a flow of short circuit current and if they are in *off* state, then it will lead to an undefined potential at the output of each leg.

The dead-time effect, IGBT saturation voltage and diode forward voltage drop has been neglected to keep the model simple. Considering negative DC-bus N as reference, the space vector of the converter output voltage is defined as:

$$\boldsymbol{u}_{\mathrm{c}}^{\mathrm{s}} = \frac{2}{3}(u_{aN} + e^{j2\pi/3}u_{bN} + e^{j4\pi/3}u_{cN}) \tag{2.1}$$

where u_{aN}, u_{bN} and u_{cN} are phase-to-neutral (N) voltages of the converter.

The switching states defined in the Table 2.1 gives the following converter voltages:

$$u_{aN} = S_a \; u_{dc} \tag{2.2}$$
$$u_{bN} = S_b \; u_{dc} \tag{2.3}$$
$$u_{cN} = S_c \; u_{dc} \tag{2.4}$$

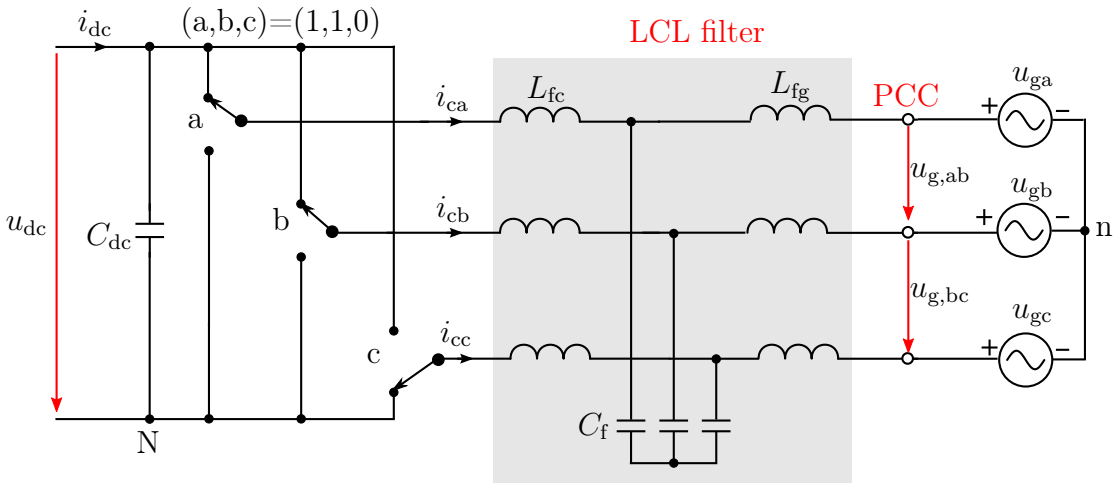

Figure 2.1: Change-over switch model of a three-phase two-level grid converter equipped with an LCL filter.

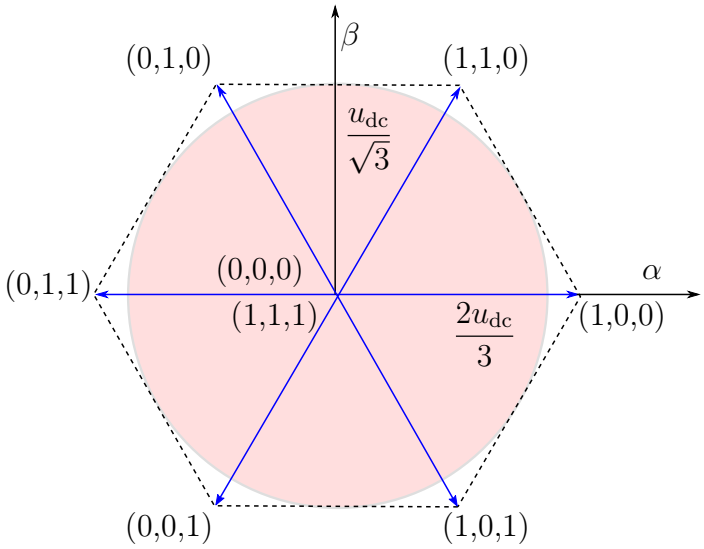

Figure 2.2: Voltage vectors in stationary $\alpha\beta$ coordinates.

where u_{dc} is the DC-bus voltage.

The Clarke transformation (2.1) applied to the switching states given in Table 2.1, results in seven different voltage vectors (six active and two zero switching states) which are visualized in Fig. 2.2.

The Park transformation is used to transform from stationary coordinates to dq coordinates. The converter voltage $\boldsymbol{u}_c^s$ in $\alpha\beta$ frame is rotated by an angle θ_g to produce converter voltage $\boldsymbol{u}_c$ in synchronous reference (dq) frame. Park transformation is given by

$$\boldsymbol{u}_c = \boldsymbol{u}_c^s e^{-j\theta_g} \tag{2.5}$$

where θ_g is the grid voltage angle as shown in Fig. 2.3.

Table 2.1: Switching states and voltage vectors in $\alpha\beta$ coordinates.

S_a	S_b	S_c	Voltage Vectors	
0	0	0	0	$\mathbf{V}_1$
1	0	0	$\frac{2}{3}u_{dc}$	$\mathbf{V}_2$
1	1	0	$\frac{1}{3}u_{dc} + j\frac{\sqrt{3}}{3}u_{dc}$	$\mathbf{V}_3$
0	1	0	$-\frac{1}{3}u_{dc} + j\frac{\sqrt{3}}{3}u_{dc}$	$\mathbf{V}_4$
0	1	1	$-\frac{2}{3}u_{dc}$	$\mathbf{V}_5$
0	0	1	$-\frac{1}{3}u_{dc} - j\frac{\sqrt{3}}{3}u_{dc}$	$\mathbf{V}_6$
1	0	1	$\frac{1}{3}u_{dc} - j\frac{\sqrt{3}}{3}u_{dc}$	$\mathbf{V}_7$
1	1	1	0	$\mathbf{V}_8$

2.2 LCL filter model

The switches of a grid converter turn *on* and *off* at high switching frequency f_{sw} and chops the dc-link voltage into a train of high frequency voltage pulses. By controlling the width of these pulses a sinusoidal ac current can be synthesized. However, this high frequency switching transition (2-15 kHz for low-voltage medium or high-power applications) causes higher order harmonics, resulting in a distorted converter current. In order to meet the harmonic distortion limit as per IEEE 519-2014 shown in Table 2.2, an LCL filter is introduced between the grid converter and the utility grid. The LCL filter filters the converter current and feeds smooth sinusoidal current into the grid. This section explains the continuous and discrete-time model of an LCL filter.

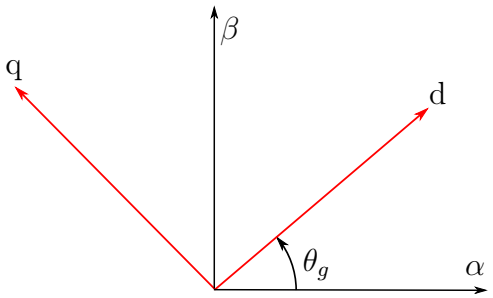

Figure 2.3: Representation of dq and $\alpha\beta$ reference frame.

Table 2.2: Maximum odd harmonic current distortion in percent of rated current I_{fun} for distribution systems (120 V - 69 kV) according to IEEE-519 [11]. I_{sc} defines the maximum short-circuit current and n defines the harmonic number. Even harmonics are limited to 25% of the odd harmonics.

I_{sc}/I_{fun}	$3 \leq \|n\| <11$	$11 \leq \|n\| <17$	$17 \leq \|n\| <23$	$23 \leq \|n\| <35$	$35 \leq \|n\| < 50$	THD
< 20	4.0	2.0	1.5	0.6	0.3	5.0
20<50	7	3.5	2.5	1.0	0.5	8.0
50<100	10	4.5	4.0	1.5	0.7	12.0
100<1000	12.0	5.5	5.0	2.0	1.0	15.0
>1000	15.0	7.0	6.0	2.5	1.4	20.0

2.2.1 Continuous time model

The losses of the filter are neglected because the losses are negligible for higher power rating and a filter without losses represents the worst-case scenario [1]. The grid impedance is also neglected in this study. The grid voltage $\boldsymbol{u}_{\mathrm{g}}$ is fixed with the $d-$axis so that $\boldsymbol{u}_{\mathrm{g}} = u_{gd} + j0$. The state vector $\mathbf{x}$ is a selection of converter current $\boldsymbol{i}_{\mathrm{c}}$, voltage across the filter capacitor $\boldsymbol{u}_{\mathrm{f}}$ and grid current $\boldsymbol{i}_{\mathrm{g}}$ i.e. $\mathbf{x} = [\boldsymbol{i}_{\mathrm{c}}\ \boldsymbol{u}_{\mathrm{f}}\ \boldsymbol{i}_{\mathrm{g}}]^{\mathrm{T}}$.

By applying KVL to the equivalent circuit of LCL filter shown in Fig. 2.4, we have

$$\boldsymbol{u}_{\mathrm{c}}^{\mathrm{s}} - L_{fc}\frac{d\boldsymbol{i}_{\mathrm{c}}^{\mathrm{s}}}{dt} - \boldsymbol{u}_{\mathrm{f}}^{\mathrm{s}} = 0 \tag{2.6}$$

where $\boldsymbol{u}_{\mathrm{c}}^{\mathrm{s}}$ is the converter voltage in $\alpha\beta$ coordinates and L_{fc} is converter side filter inductor. The equation (2.6) can be transformed to dq coordinates by:

$$\frac{d}{dt} \rightarrow \frac{d}{dt} + j\omega_g \tag{2.7}$$

where ω_g is the grid angular frequency. Therefore, equation (2.6) in dq coordinates is given by:

$$\boldsymbol{u}_{\mathrm{c}} - L_{fc}\frac{d\boldsymbol{i}_{\mathrm{c}}}{dt} - j\omega_g L_{fc}\boldsymbol{i}_{\mathrm{c}} - \boldsymbol{u}_{\mathrm{f}} = 0 \tag{2.8}$$

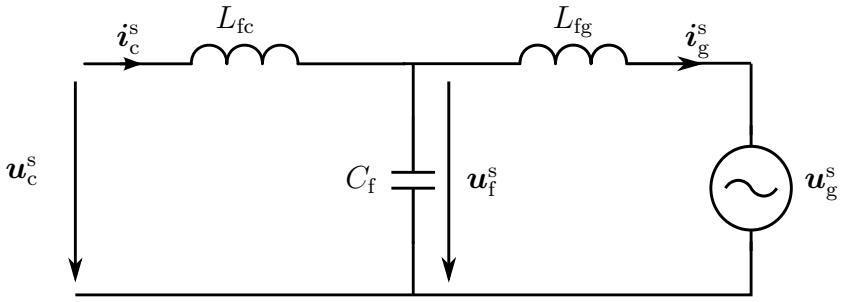

Figure 2.4: Equivalent circuit model for LCL filter in stationary $\alpha\beta$ coordinates.

where, $\boldsymbol{u}_\mathrm{c}$ is the converter voltage in dq coordinates and L_{fc} is the converter side filter inductor. Using the equation (2.8) the state $\boldsymbol{i}_\mathrm{c}$ is given by (2.9) and similarly, the expressions for other states are:

$$\frac{d\boldsymbol{i}_\mathrm{c}}{dt} = -j\omega_g \boldsymbol{i}_\mathrm{c} - \frac{\boldsymbol{u}_\mathrm{f}}{L_{fc}} + \frac{\boldsymbol{u}_\mathrm{c}}{L_{fc}} \tag{2.9}$$

$$\frac{d\boldsymbol{u}_\mathrm{f}}{dt} = \frac{\boldsymbol{i}_\mathrm{c}}{C_f} - j\omega_g \boldsymbol{u}_\mathrm{f} - \frac{\boldsymbol{i}_\mathrm{g}}{C_f} \tag{2.10}$$

$$\frac{d\boldsymbol{i}_\mathrm{g}}{dt} = \frac{\boldsymbol{u}_\mathrm{f}}{L_{fg}} - j\omega_g \boldsymbol{i}_\mathrm{g} - \frac{\boldsymbol{u}_\mathrm{g}}{L_{fg}} \tag{2.11}$$

where C_f is the filter capacitor and L_{fg} is the grid side filter inductor shown in Fig. 2.4.

The state-space equation governing the continuous-time dynamics of the converter current $\boldsymbol{i}_\mathrm{c}$ is given by:

$$\begin{aligned}
\frac{d}{dt}\underbrace{\begin{bmatrix}\boldsymbol{i}_\mathrm{c}\\ \boldsymbol{u}_\mathrm{f}\\ \boldsymbol{i}_\mathrm{g}\end{bmatrix}}_{\mathbf{x}} &= \underbrace{\begin{bmatrix}-j\omega_g & -\frac{1}{L_{fc}} & 0\\ \frac{1}{C_f} & -j\omega_g & -\frac{1}{C_f}\\ 0 & \frac{1}{L_{fg}} & -j\omega_g\end{bmatrix}}_{\mathbf{A}}\begin{bmatrix}\boldsymbol{i}_\mathrm{c}\\ \boldsymbol{u}_\mathrm{f}\\ \boldsymbol{i}_\mathrm{g}\end{bmatrix} + \underbrace{\begin{bmatrix}\frac{1}{L_{fc}}\\ 0\\ 0\end{bmatrix}}_{\mathbf{B}_\mathrm{c}}\boldsymbol{u}_\mathrm{c} + \underbrace{\begin{bmatrix}0\\ 0\\ -\frac{1}{L_{fg}}\end{bmatrix}}_{\mathbf{B}_\mathrm{g}}\boldsymbol{u}_\mathrm{g}\\
\boldsymbol{i}_\mathrm{c} &= \underbrace{\begin{bmatrix}1 & 0 & 0\end{bmatrix}}_{\mathbf{C}_\mathrm{c}}\begin{bmatrix}\boldsymbol{i}_\mathrm{c}\\ \boldsymbol{u}_\mathrm{f}\\ \boldsymbol{i}_\mathrm{g}\end{bmatrix}
\end{aligned} \tag{2.12}$$

The transfer function from the converter voltage $\boldsymbol{u}_\mathrm{c}(s)$ to the converter current $\boldsymbol{i}_\mathrm{c}(s)$ is given by:

$$\begin{aligned}
\mathbf{Y}(s) &= \mathbf{C}_\mathrm{c}(s\mathbf{I} - \mathbf{A})^{-1}\mathbf{B}_\mathrm{c}\\
&= \frac{1}{L_{fc}}\frac{(s+j\omega_g)^2 + \omega_z^2}{(s+j\omega_g)[(s+j\omega_g)^2 + \omega_p^2]}
\end{aligned} \tag{2.13}$$

where

$$\omega_p = \sqrt{\frac{L_{fc}+L_{fg}}{L_{fc}L_{fg}C_f}}; \quad \omega_z = \sqrt{\frac{1}{L_{fg}C_f}} \tag{2.14}$$

are the resonant frequency and the anti-resonant frequency of the LCL filter, respectively.

2.2.2 Discrete-time model

The control algorithm has to be implemented on a digital microprocessor, so discrete model of the LCL filter is essential. The continuous-time models are well established and can be used to make discrete-time equivalents. The continuous-time models can

be discretized using Euler or Tustin approximation. The approximation made using these emulation method are fairly accurate for high sampling frequency f_s. But, the performance of the emulation based controllers degrades as the sampling frequency f_s is decreased. Therefore, exact discrete-time model is required to improve the controller performance at low f_s.

Different methods to discretize the continuous-time LCL filter model have been explained in the literature [1, 2]. A ZOH in stationary coordinates has been used to discretize the state space model given in equation (2.12). The following assumptions are made in the derivation of the discrete model:

(i) The grid angular frequency ω_g is considered constant between two successive sampling instant.

(ii) The filter parameters (L_{fc}, L_{fg} and C_f) are considered to be constant between two successive sampling instant.

Based upon these assumptions, the converter voltage $\boldsymbol{u}_{\mathrm{c}}^{\mathrm{s}}(t)$ is considered to be piece-wise constant during each sampling instant in stationary coordinates, corresponding to a ZOH in stationary coordinates. If T_s is the sampling time and k is discrete time index then $\boldsymbol{u}_{\mathrm{c}}(t)$ is considered to be constant between $kT_s < t < (k+1)T_s$ i.e., converter voltage is time invariant in stationary coordinates and time variant in synchronous coordinates. The exact discrete-time model is given below:

$$\begin{aligned} \mathbf{x}(k+1) &= \boldsymbol{\Phi}\mathbf{x}(k) + \boldsymbol{\Gamma}_{\mathrm{c}}\boldsymbol{u}_{\mathrm{c}}(k) + \boldsymbol{\Gamma}_{\mathrm{g}}\boldsymbol{u}_{\mathrm{g}}(k) \\ \boldsymbol{i}_{\mathrm{c}}(k) &= \mathbf{C}_{\mathrm{c}}\mathbf{x}(k) \end{aligned} \tag{2.15}$$

where the system matrices are given by

$$\boldsymbol{\Phi} = \mathrm{e}^{\mathbf{A}T_s},\ \boldsymbol{\Gamma}_{\mathrm{c}} = \left(\int_0^{T_s} \mathrm{e}^{\mathbf{A}\tau}\mathrm{e}^{-j\omega_g(T_s-\tau)}d\tau\right)\mathbf{B}_{\mathrm{c}},\ \boldsymbol{\Gamma}_{\mathrm{g}} = \left(\int_0^{T_s} \mathrm{e}^{\mathbf{A}\tau}d\tau\right)\mathbf{B}_{\mathrm{g}} \tag{2.16}$$

The factor $e^{-j\omega_g(T_s-\tau)}$ inside the integral of $\boldsymbol{\Gamma}_{\mathrm{c}}$ originates from ZOH modelled in stationary coordinates. The closed form expression of the matrices in equation 2.15 are given in Appendix A.

2.3 Grid synchronization (Phase locked loop)

Grid synchronization of a grid converter requires estimation of grid voltage phase angle. A phase locked loop (PLL) provides information about the phase-angle and amplitude of the fundamental grid voltage. Block diagram for PLL used in grid synchronization is shown in Fig. 2.5. The aim of PLL is to drive the $q-$component of the grid-voltage to zero such that $\boldsymbol{u}_{\mathrm{g}} = u_{gd} + j0$.

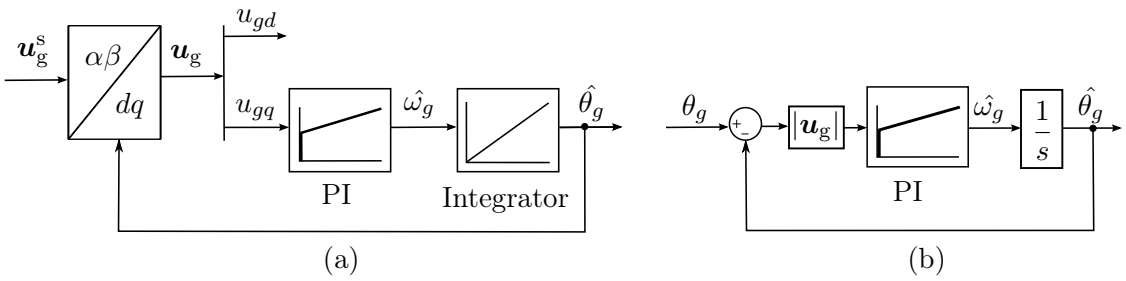

Figure 2.5: (a)Phase locked loop for grid synchronization. (b)Linearized block diagram for PLL.

The q-component u_{gq} of the grid voltage $\boldsymbol{u}_{\mathrm{g}}$ is

$$\begin{aligned} u_{gq} &= -u_{g\alpha} cos\ \hat{\theta}_g + u_{g\beta} sin\ \hat{\theta}_g \\ &= -u_g cos\ \theta_g\ sin\ \hat{\theta}_g + u_g sin\ \theta_g\ cos\ \hat{\theta}_g \\ &= u_g sin(\theta_g - \hat{\theta}_g) \approx u_g(\theta_g - \hat{\theta}_g) \end{aligned} \tag{2.17}$$

where $u_{g\alpha}$ and $u_{g\beta}$ are the α and β components of the grid voltage $\boldsymbol{u}_{\mathrm{g}}^{\mathrm{s}}$ respectively, and $\hat{\theta}_g$ is the angle estimated by PLL.

Similarly, the d-component of the grid voltage $\boldsymbol{u}_{\mathrm{g}}$ is

$$\begin{aligned} u_{gd} &= u_{g\alpha} cos\ \hat{\theta}_g + u_{g\beta} sin\ \hat{\theta}_g \\ &= u_g cos(\theta_g - \hat{\theta}_g) \end{aligned}$$

Therefore, when $\theta_g = \hat{\theta}_g$ the q-component u_{gq} will be driven to zero and the d-component u_{gd} will be equal to the amplitude of the grid voltage $\boldsymbol{u}_{\mathrm{g}}$. The linearized block diagram of PLL, taking into account equation (2.17), is shown in Fig. 2.5 (b).

The transfer function $\mathrm{G_{PLL}}(s)$ from θ_g to $\hat{\theta}_g$ is

$$\mathrm{G_{PLL}}(s) = \frac{u_g(k_p s + k_i)}{s^2 + u_g k_p s + u_g k_i} \tag{2.18}$$

The poles of the second-order transfer function is given by

$$s^2 + 2\zeta\omega_o s + \omega_o^2 \tag{2.19}$$

where ζ is the damping ratio and ω_o is the natural frequency. The controller gains k_p and k_i is obtained by comparing the poles of the transfer function $\mathrm{G_{PLL}}(s)$ with equation (2.19).

$$k_p = \frac{2\zeta\omega_o}{u_g}\ ; k_i = \frac{\omega_o^2}{u_g} \tag{2.20}$$

The natural frequency ω_o is tuned to $2\pi(20)$ rad/s so that the noise and harmonics above 20 Hz is filtered out. The damping ratio ζ is tuned to 1. The estimated angle and actual angle of the grid voltage $\boldsymbol{u}_{\mathrm{g}}$ is shown in Fig. 2.6.

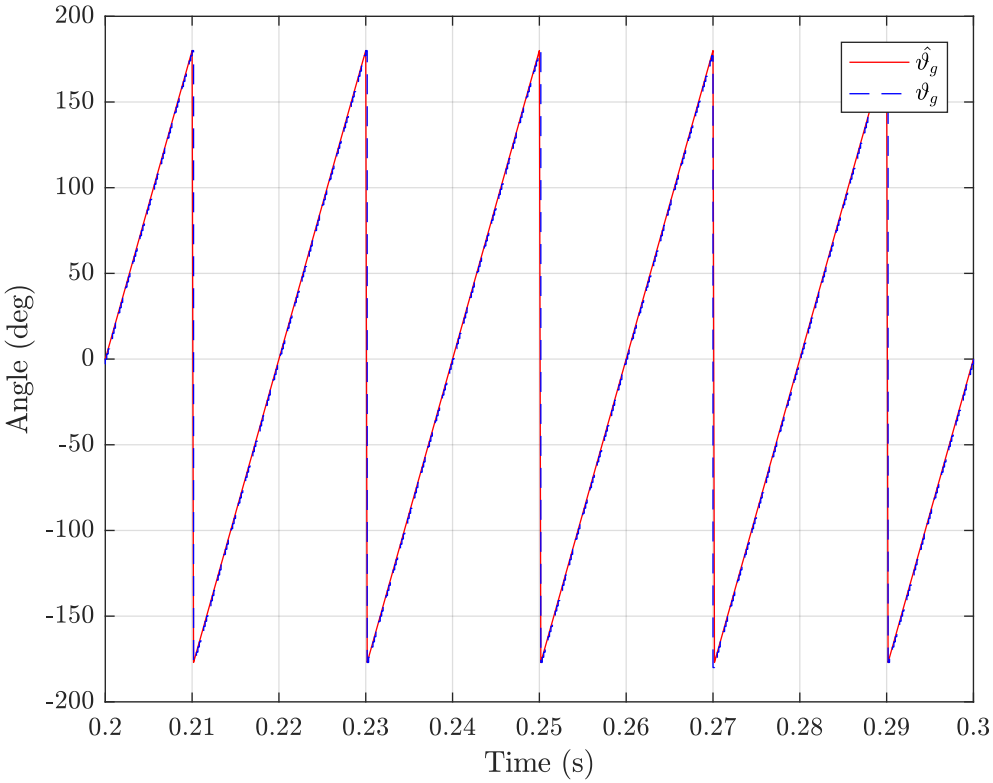

Figure 2.6: Actual angle and estimated angle of grid voltage $\boldsymbol{u}_{\mathrm{g}}$.

3 Finite-set model predictive current control

FS-MPC departs from PWM technology and directly optimizes the switching states of the VSC to implement the control action. This chapter explains the scheme of FS-MPC used for current control of a three-phase two-level VSC and the concept of receding horizon and long horizon.

3.1 Model predictive current control

FS-MPC uses a control strategy based upon the finite number of switching states that can be generated by a grid converter and a system model that can be used to predict the system state for each switching state. The appropriate switching state is selected, based upon a selection criterion. This selection criterion consists of a cost function that will predict the future values of the variables to be controlled. Prediction of future values of the variable to be controlled is done for each switching state. The state which minimizes the cost function is applied to the converter.

The basic control design can be formulated into the following steps:

- Design a converter model and define its possible switching states.
- Design a discrete model for predicting current behaviour.
- Define a cost function g.
- Define the minimization criteria for current control.

3.2 Discrete-time model for current prediction

This section describes the use of the discrete-model explained in section 2.2.2 for a sampling time T_s. The discrete model will be used to predict the future value of the state vector $\mathbf{x} = [\boldsymbol{i}_\mathrm{c}\ \boldsymbol{u}_\mathrm{f}\ \boldsymbol{i}_\mathrm{g}]^\mathrm{T}$ at any sampling instant.

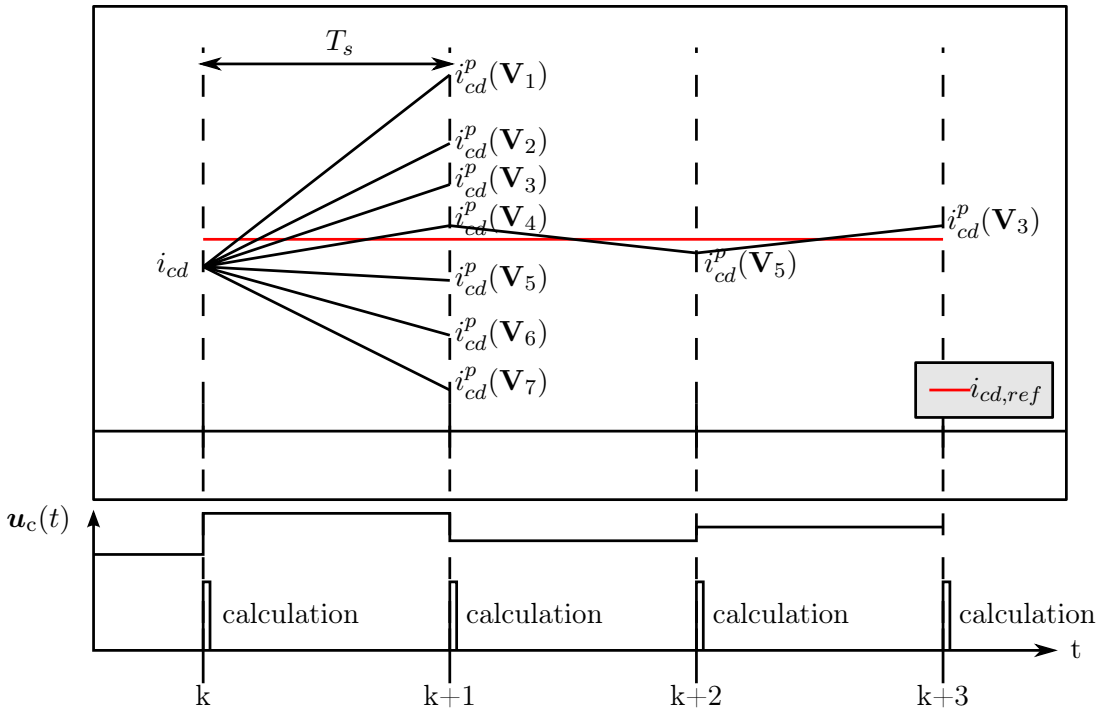

Figure 3.1: Operation of FS model predictive current control.

The current reference in $\alpha\beta$ coordinates will be alternating, therefore an extrapolation method, such as Lagrange polynomials, is needed to accurately predict the future current references for calculating errors at present time instant. Since, the extrapolation process requires past values of the current reference, it will produce oscillation in case of a step change in current reference. These unwanted oscillations will have a negative effect in the transient response of the current controller [7]. To avoid this issue the study of this thesis will be done in rotating dq reference frame.

The contribution of discrete model in the operation of FS model predictive current control is shown in Fig. 3.1. For simplification, only d-component of converter current $\boldsymbol{i}_c$ is used and the calculation time for voltage vectors is neglected. At any time instant k, the state of the system is measured. Using these measurements and equation (2.15), the future converter current i^p_{cd} is predicted for time instant $k+1$, for all the voltage vectors described in Table 2.1.

In the Fig. 3.1, it can be seen that the vector $\mathbf{V}_4$ takes the current i_{cd} closest to the reference current $i_{cd,ref}$ at time instant $k+1$. if the switching state (S_a, S_b, S_c) = (0, 1, 0) corresponding to the voltage vector $\mathbf{V}_4$ is applied to the converter at time instant k, then the current i_{cd} will follow the trajectory of the predicted current i^p_{cd}. Therefore, voltage vector $\mathbf{V}_4$ minimizes the error $(i_{cd,ref}(k+1) - i^p_{cd}(k+1))$ at time instant k. Similarly, voltage vector $\mathbf{V}_5$ and $\mathbf{V}_3$ minimizes the error at time instant $k+1$ and $k+2$ respectively; thus, defining the trajectory of the converter current i_{cd}.

3.3 Cost function

The objective of a current controller is to reduce the error between measured and reference current. In FS model predictive current control, this can be accomplished using a cost function which aims in minimizing the error between measured and reference current. A cost function can be defined as an absolute value or square value for one sampling period [2]:

$$g = |\boldsymbol{i}_{\mathrm{c,ref}}(k+1) - \boldsymbol{i}_{\mathrm{c}}^{\mathrm{p}}(k+1)| \tag{3.1}$$

$$g = |\boldsymbol{i}_{\mathrm{c,ref}}(k+1) - \boldsymbol{i}_{\mathrm{c}}^{\mathrm{p}}(k+1)|^2 \tag{3.2}$$

where $\boldsymbol{i}_{\mathrm{c,ref}}$ is the converter reference current and $\boldsymbol{i}_{\mathrm{c}}^{\mathrm{p}}$ is the converter current predicted at time instant k for time instant $k+1$. The converter reference current $\boldsymbol{i}_{\mathrm{c,ref}}$ at time instant $k+1$ is assumed to be same as $\boldsymbol{i}_{\mathrm{c,ref}}$ at time instant k. This will produce one sample delay in current reference tracking. Since the sampling frequency is high enough, it will produce negligible effect on the bandwidth of the controller. Absolute error and squared error gives almost the same performance for reference tracking if the cost function considers single variable. In multi variable constraint the results can be different. In this thesis squared error cost function has been used for current reference tracking. The cost function can include several constraints, like reduction in switching frequency [2, 14], DC bus voltage control [3], resonance damping [2, 9], depending on the control requirement. Adding these constraints to the cost function penalizes the cost function for certain switching states.

A block diagram representing FS-MPC control strategy applied to a three-phase VSC for current control is shown in Fig. 3.2 and flow diagram for different tasks performed by the current controller is shown in Fig. 3.3.

3.4 Computation delay

FCS-MPC has the flexibility to include various constraints and control different types of variables by including them in the cost function as per control requirement. However, the algorithms developed based upon FCS-MPC strategy requires intense calculation [15].The calculation burden produces a delay of one sampling instant between the calculation and actuation of the optimal switching state.

To illustrate this behaviour, only d-component of the converter current i_{cd} is considered as the voltage vectors produce only three different values for d-component shown in Fig. 3.4. The dashed line represents i_{cd}^{p}, the predicted values of the converter current, showing the various trajectories that i_{cd} could take. The red line represents the d-component of the reference current $i_{cd,ref}$. The solid black line represents the actual trajectory taken by i_{cd} after applying the optimal converter voltage $\boldsymbol{u}_{\mathrm{c}}$ obtained by minimizing the cost function (3.2).

In the ideal case, the state measurements are done at time instant k. The switching state that minimizes the cost function (3.2) based upon the predicted

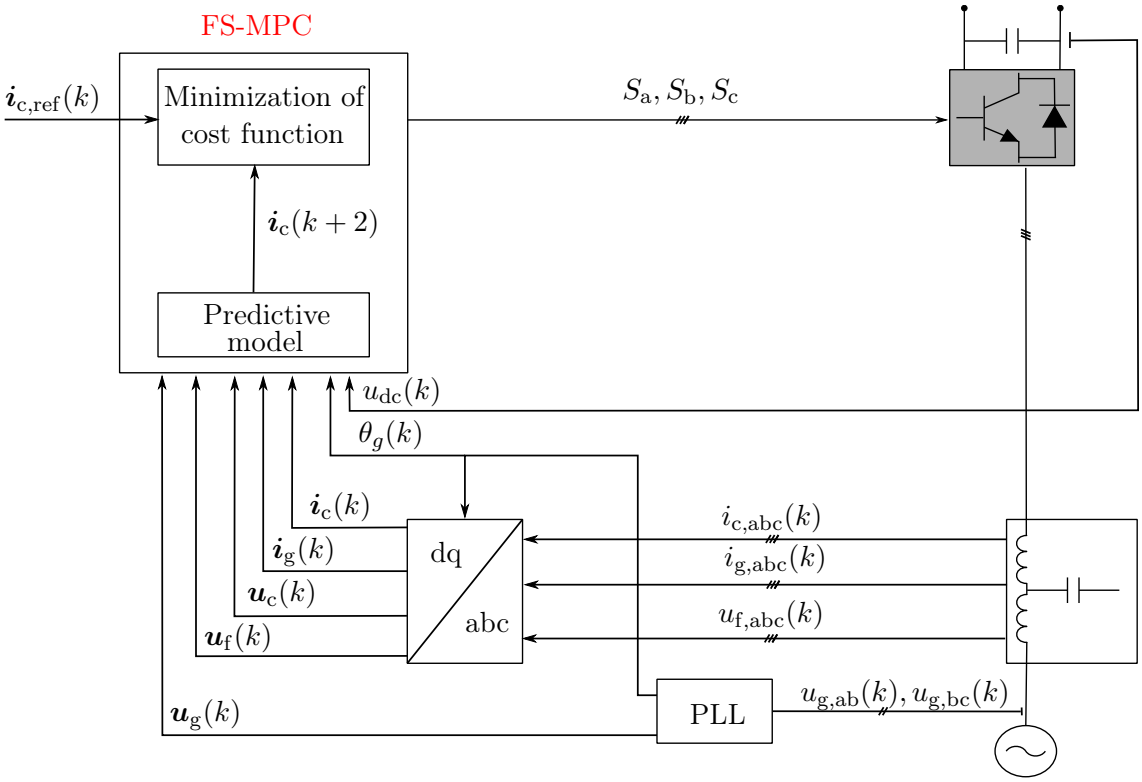

Figure 3.2: Setup for FS model predictive current control of a three-phase grid converter equipped with an LCL filter.

values of i_{cd} is calculated instantaneously and applied at time instant k. Then, i_{cd} reaches the predicted value at time instant $k+1$.

A three-phase two level VSC has seven different voltage vectors. The prediction of $i_{cd}(k+1)$ involves transformation of voltage vectors into dq reference frame and then seven different values of i_{cd} are computed based upon transformed voltage vectors. The cost function is then evaluated seven times to find the optimal switching state. These computation requires considerable amount of time and the speed of the microprocessor used for control. Hence, the computation time cannot be neglected.

This delay can be compensated by taking into account the calculation time and applying the optimal switching state at next sampling instant [15]. The method used to compensate calculation delay is graphically illustrated in Fig. 3.4. The switching state is applied based upon the calculation at time instant $k-1$ and the states are measured simultaneously at time instant k. The converter current $i_{cd}(k+1)$ is calculated at time instant k based upon the applied switching state. The converter current $i^{p}_{cd}(k+2)$ is predicted for all the seven switching states at time instant k. The cost function is evaluated for time instant $k+2$ and the optimal switching state obtained by minimizing the cost function at time instant k is applied at time instant

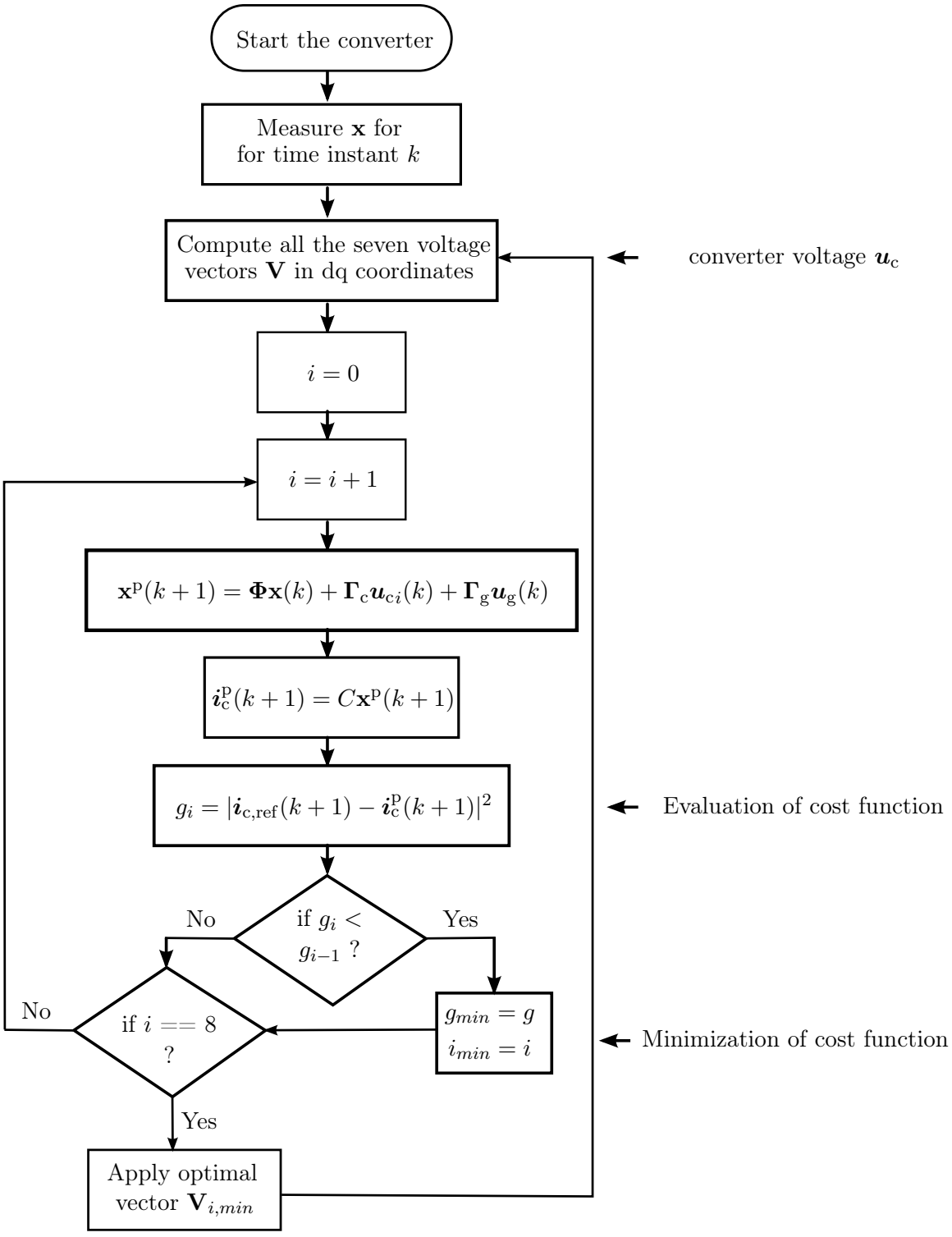

Figure 3.3: Flowchart of a typical FS model predictive current controller.

$k+1$. Thus, the predictions are shifted one step forward in time:

$$\mathbf{x}(k+1) = \mathbf{\Phi}\mathbf{x}(k) + \mathbf{\Gamma}_c\boldsymbol{u}_c(k) + \mathbf{\Gamma}_g\boldsymbol{u}_g(k) \tag{3.3}$$

$$\mathbf{x}(k+2) = \mathbf{\Phi}\mathbf{x}(k+1) + \mathbf{\Gamma}_c\boldsymbol{u}_{ci}(k+1) + \mathbf{\Gamma}_g\boldsymbol{u}_g(k) \tag{3.4}$$

$$\boldsymbol{i}_c^p(k+2) = \mathbf{C}_c\mathbf{x}(k+2) \tag{3.5}$$

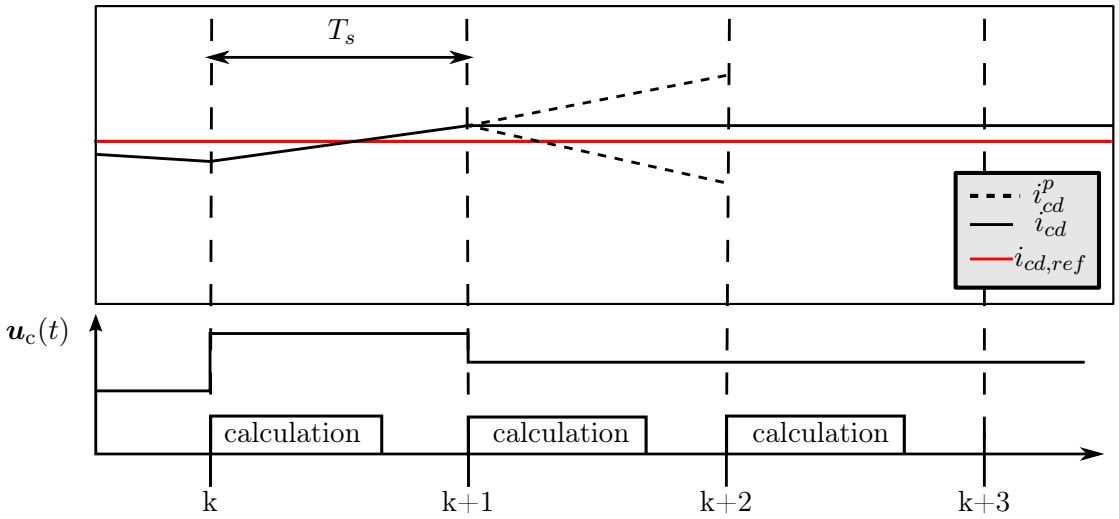

Figure 3.4: Operation of FS model predictive current control with delay compensation: long calculation time (practical case) [15]

where $\boldsymbol{u}_c(k)$ is the optimal converter voltage calculated at time instant $k-1$ and $\boldsymbol{u}_{ci}(k+1)$ $(i \rightarrow\ 1\ to\ 7)$ represents all the seven different voltage vectors shown in Table 2.1 transformed in dq coordinates using

$$\boldsymbol{u}_c(k+1) = \boldsymbol{u}_c^s(k) e^{-j(\theta_g + T_s \omega_g)}. \tag{3.6}$$

3.5 Switching frequency

The switching frequency of the converter in a FS-MPC controller is variable and is dependent upon the sampling frequency of the control algorithm, the load characteristics and the operating point [7]. The switching losses are not only depending upon the present values of current and voltage but also on the frequency at which the converter is operating. Therefore, it is desirable to reduce the switching frequency while maintaining THD within limits. FS-MPC facilitates in reducing the switching frequency directly by adding a constraint to the cost function that punishes the current trajectories with many switching transition. The resulting cost function that defines the number of switching commutation from time instant $k-1$ to k is

$$g = \lambda_{sw} \|\mathbf{S}(k) - \mathbf{S}(k-1)\|^2 \tag{3.7}$$

where $\mathbf{S} = [S_a\ S_b\ S_c]^{\mathrm{T}}$ represents the switching state vector and λ_{sw} is the weight assigned to this constraint. By increasing λ_{sw}, switching frequency can be decreased [10].

The average switching frequency can be calculated by averaging over individual switching frequency of 6 active states [16]. The average switching frequency per

semiconductor device is given by:

$$f_{sw} = \lim_{N\to\infty} \frac{1}{6NT_s} \sum_{k=0}^{N-1} \|\mathbf{S}(k) - \mathbf{S}(k-1)\|^2 \tag{3.8}$$

The converter current feedback has the tendency to make the system unstable if the resonance frequency is high in comparison with the switching frequency [17]. In FS-MPC the average switching frequency f_{sw} is directly proportional to the sampling frequency. Therefore, as a rule of thumb the sampling frequency of the system is adjusted to make the average switching frequency f_{sw} twice the resonance frequency ω_p of the LCL filter.

3.6 Prediction horizon

The number of time-steps the controller looks into the future is termed as prediction horizon N. An example of state propagation flow graph having a horizon of $N = 2$ is shown in Fig. 3.5. The cost function g is minimized considering the predicted states $\mathbf{x}^{\mathrm{p}}(k+2)$ and $\mathbf{x}^{\mathrm{p}}(k+3)$. It can be seen from the figure that the amount of calculation increases with the increase in the prediction horizon. Several strategies to obtain long prediction horizon are explained in [2, 19, 20].

A prediction sequence (e.g. CECE) which takes place within each prediction, is introduced to FS-MPC, consisting of a control step (C) and extension step (E) [2]. In step C, all the seven switching vectors are evaluated to predict the state at the next time step and in step E, the switching state from the previous time instant is kept constant to a later point in time. The step E can be done through extrapolation or by using the discrete-time model (2.15).

The computational burden increases exponentially with the increase in the prediction horizon which makes it difficult to solve most of the optimization problem related to MPC. At the same time, the sampling frequency of the system is also high, which makes the solution of long prediction problems very challenging.

The state space model can be used to form a compact form for the prediction of converter current for up to horizon N.

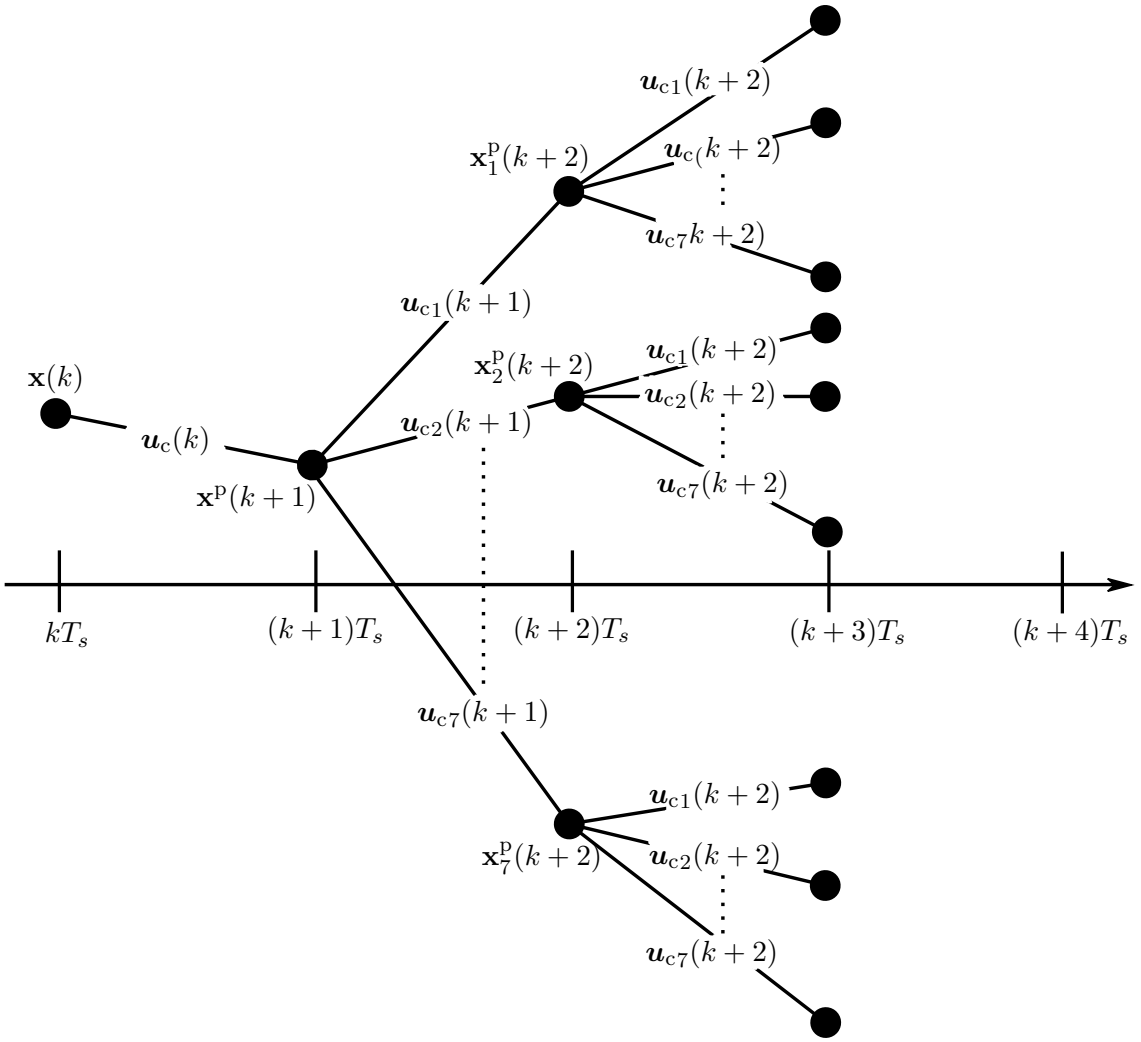

Figure 3.5: State propagation flow graph of a FCS-MPC process posed in the *dq* reference frame [21]

$$\underbrace{\begin{bmatrix}\boldsymbol{y}(k+1)\\ \boldsymbol{y}(k+2)\\ \vdots\\ \boldsymbol{y}(k+N)\end{bmatrix}}_{\mathbf{Y}} = \underbrace{\begin{bmatrix}\mathbf{C}_c\boldsymbol{\Phi}\\ \mathbf{C}_c\boldsymbol{\Phi}^2\\ \vdots\\ \mathbf{C}_c\boldsymbol{\Phi}^N\end{bmatrix}}_{\boldsymbol{\Gamma}}\mathbf{x}(k) + \underbrace{\begin{bmatrix}\mathbf{C}_c\boldsymbol{\Gamma}_c & 0 & \cdots & 0\\ \mathbf{C}_c\boldsymbol{\Phi}\boldsymbol{\Gamma}_c & \mathbf{C}_c\boldsymbol{\Gamma}_c & \cdots & 0\\ \vdots & \vdots & \ddots & \cdots\\ \mathbf{C}_c\boldsymbol{\Phi}^{N-1}\boldsymbol{\Gamma}_c & \mathbf{C}_c\boldsymbol{\Phi}^{N-2}\boldsymbol{\Gamma}_c & \cdots & \mathbf{C}_c\boldsymbol{\Gamma}_c\end{bmatrix}}_{\boldsymbol{\Upsilon}}\underbrace{\begin{bmatrix}\boldsymbol{u}_c(k)\\ \boldsymbol{u}_c(k+1)\\ \vdots\\ \boldsymbol{u}_c(k+N)\end{bmatrix}}_{\mathbf{U}_c}$$

$$+ \underbrace{\begin{bmatrix}\mathbf{C}_c\boldsymbol{\Gamma}_c & 0 & \cdots & 0\\ \mathbf{C}_c\boldsymbol{\Phi}\boldsymbol{\Gamma}_g & \mathbf{C}_c\boldsymbol{\Gamma}_g & \cdots & 0\\ \vdots & \vdots & \ddots & \cdots\\ \mathbf{C}_c\boldsymbol{\Phi}^{N-1}\boldsymbol{\Gamma}_g & \mathbf{C}_c\boldsymbol{\Phi}^{N-2}\boldsymbol{\Gamma}_g & \cdots & \mathbf{C}_c\boldsymbol{\Gamma}_g\end{bmatrix}}_{\boldsymbol{\Psi}}\underbrace{\begin{bmatrix}\boldsymbol{u}_g(k)\\ \boldsymbol{u}_g(k+1)\\ \vdots\\ \boldsymbol{u}_g(k+N)\end{bmatrix}}_{\mathbf{U}_g}$$

$$\mathbf{Y}(k) = \begin{bmatrix}\boldsymbol{i}_c(k+1) & \boldsymbol{i}_c(k+2) & \dots & \boldsymbol{i}_c(k+N)\end{bmatrix}^{\mathrm{T}}$$

$$\mathbf{Y}(k) = \boldsymbol{\Gamma}\mathbf{x}(k) + \boldsymbol{\Upsilon}\mathbf{U}_c(k) + \boldsymbol{\Psi}\mathbf{U}_g(k) \tag{3.9}$$

Similarly, the constraint for reducing the switching frequency is modified to impose restriction on the entire horizon

$$g = \lambda_{sw} \| \begin{bmatrix} \mathbf{I}_3 & \mathbf{0}_{3\times3} & \cdots & \mathbf{0}_{3\times3} \\ -\mathbf{I}_3 & \mathbf{I}_3 & \cdots & \mathbf{0}_{3\times3} \\ \mathbf{0}_{3\times3} & -\mathbf{I}_3 & \cdots & \mathbf{0}_{3\times3} \\ \vdots & \vdots & & \vdots \\ \mathbf{0}_{3\times3} & \mathbf{0}_{3\times3} & \cdots & \mathbf{I}_3 \end{bmatrix} \begin{bmatrix} \mathbf{S}(k) \\ \mathbf{S}(k+1) \\ \mathbf{S}(k+2) \\ \vdots \\ \mathbf{S}(k+N) \end{bmatrix} + \begin{bmatrix} \mathbf{I}_3 \\ \mathbf{0}_{3\times3} \\ \mathbf{0}_{3\times3} \\ \vdots \\ \mathbf{0}_{3\times3} \end{bmatrix} \mathbf{S}(k-1) \|^2 \tag{3.10}$$

3.7 Optimal control system

The cost function (3.2), taking into account (3.9), can be re-written in a quadratic form

$$g = \left[\mathbf{Y}_{\text{ref}}(k) - \mathbf{Y}(k)\right]^{\text{T}} \left[\mathbf{Y}_{\text{ref}}(k) - \mathbf{Y}(k)\right] \tag{3.11}$$

Under optimal control, the reference current is equal to the actual current. Using equation (3.9) and (3.11) expressed in matrix form, the vector $[\mathbf{F}_{dq}(k)] = [\boldsymbol{\Upsilon}\mathbf{U}_{\text{c}}^{\text{opt}}(k)]$ is defined as:

$$[\mathbf{F}_{dq}(k)] = [\mathbf{Y}_{\text{ref}}(k) - \boldsymbol{\Gamma}\mathbf{x}(k) - \boldsymbol{\Psi}\mathbf{U}_{\text{g}}(k)] \tag{3.12}$$

The objective cost function in terms of control is

$$J = [\mathbf{F}_{dq}(k) - \boldsymbol{\Upsilon}\mathbf{U}_{\text{c}}(k)]^T [\mathbf{F}_{dq}(k) - \boldsymbol{\Upsilon}\mathbf{U}_{\text{c}}(k)] \tag{3.13}$$

The objective function J can be minimized as a least square minimization problem. Taking partial derivative of the objective cost function J, the optimal voltage vector in dq coordinates is defined as:

$$\mathbf{U}_{\text{c,unc}}(k) = \boldsymbol{\Upsilon}^{-1}[\mathbf{Y}_{\text{ref}}(k) - \boldsymbol{\Gamma}\mathbf{x}(k) - \boldsymbol{\Psi}\mathbf{U}_{\text{g}}(k)] \tag{3.14}$$

where $\mathbf{U}_{\text{c,unc}}$ is the optimal control without any restriction on the converter voltage [22]. The partial derivative of J with respect to converter voltage is given in Appendix B. The unconstrained optimal control can be used to define the objective function for constrained control problem:

$$J = [\mathbf{U}_{\text{c}}(k) - \mathbf{U}_{\text{c,unc}}(k)]^{\text{T}} \boldsymbol{\Upsilon}^{\text{T}} \boldsymbol{\Upsilon} [\mathbf{U}_{\text{c}}(k) - \mathbf{U}_{\text{c,unc}}(k)] \tag{3.15}$$

The optimal converter voltage that will minimize the cost function (3.15) can be obtained using exhaustive search, modified sphere decoding algorithm [10] or trajectory prediction using candidate sequence [20, 23] for longer horizon.

3.8 Reference calculation

The feedback current used in this thesis for the current controller is converter current $\boldsymbol{i}_{\mathrm{c}}$. The converter current $\boldsymbol{i}_{\mathrm{c}}$ is used to control the grid current $\boldsymbol{i}_{\mathrm{g}}$ and grid power indirectly. Using equation (2.9) in steady-state the converter current $\boldsymbol{i}_{\mathrm{c}}$ is given by

$$\boldsymbol{i}_{\mathrm{c}} = (1 - \omega_g^2 L_{fg} C_f)\boldsymbol{i}_{\mathrm{g}} + j\omega_g C_f \boldsymbol{u}_{\mathrm{g}} \tag{3.16}$$

The $d-$axis and $q-$axis reference is calculated by taking real and imaginary part of the equation (3.16).

$$\begin{aligned} i_{cd,ref} &= (1 - \omega_g^2 L_{fg} C_f) i_{gd} \\ i_{cq,ref} &= (1 - \omega_g^2 L_{fg} C_f) i_{gq} + \omega_g C_f u_{gd} \end{aligned} \tag{3.17}$$

The real and reactive power at PCC is given by

$$\begin{aligned} p_g &= \frac{3}{2}\mathrm{Re}\{\boldsymbol{u}_{\mathrm{g}} \boldsymbol{i}_{\mathrm{g}}{}^{*}\} = \frac{3}{2} u_g i_{gd} \\ q_g &= \frac{3}{2}\mathrm{Im}\{\boldsymbol{u}_{\mathrm{g}} \boldsymbol{i}_{\mathrm{g}}{}^{*}\} = -\frac{3}{2} u_g i_{gq} \end{aligned} \tag{3.18}$$

where * denotes the complex conjugate.

The displacement power factor is considered as unity ($i_{gq} = 0$) and the converter is assumed to be lossless. The real and reactive power at converter output is given by

$$\begin{aligned} p_c &= \frac{3}{2}\mathrm{Re}\{\boldsymbol{u}_{\mathrm{c}} \boldsymbol{i}_{\mathrm{c}}^{*}\} = \frac{3}{2} u_g i_{gd} \\ q_c &= \frac{3}{2}\mathrm{Im}\{\boldsymbol{u}_{\mathrm{c}} \boldsymbol{i}_{\mathrm{c}}^{*}\} = \frac{3}{2}[\omega_g i_{cd}(L_{fc} i_{cd} + L_{fg} i_{gd}) + i_{cd}(\omega_g) L_{fc} i_{cq} - u_g] \end{aligned} \tag{3.19}$$

The reactive power at the converter output is non-zero due to the presence of the LCL filter components.

4 Resonance damping

LCL line filters are of third order and therefore provide an attenuation of 60 dB per decade to the harmonics (switching harmonics) appearing after the resonant frequency. With the introduction of LCL filters comes the problem of zero impedance at its resonance frequency; thus, amplifying the harmonics present at its resonant frequency. The damping of these dynamics can be achieved either by modifying filter parameters with the addition of passive elements or by modifying the structure of the controller. The first one is referred to as passive damping and the second one is referred to as active damping.

The equivalent circuit in *dq* reference frame is represented by a block diagram in Fig. 4.1, to visualize the transfer function governing the dynamics of the LCL filter. The transfer function from $\boldsymbol{u}_{\mathrm{c}}^{\mathrm{s}}(s)$ to $\boldsymbol{i}_{\mathrm{c}}^{\mathrm{s}}(s)$ is defined as:

$$\frac{\boldsymbol{i}_{\mathrm{c}}^{\mathrm{s}}(s)}{\boldsymbol{u}_{\mathrm{c}}^{\mathrm{s}}(s)} = \frac{1}{L_{fc}} \frac{s^2 + \frac{1}{L_{fg}C_f}}{s(s^2 + \frac{L_{fg}+L_{fc}}{L_{fg}L_{fc}C_f})} = \frac{1}{L_{fc}} \frac{s^2 + \omega_z^2}{s(s^2 + \omega_p^2)} \tag{4.1}$$

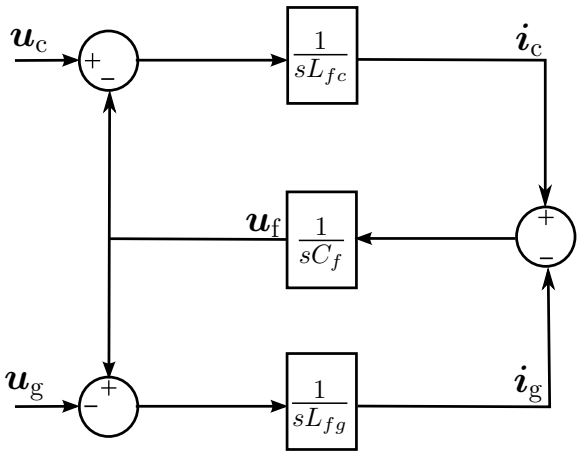

Figure 4.1: Block diagram for equivalent circuit of LCL filter in stationary coordinates, neglecting filter losses [13].

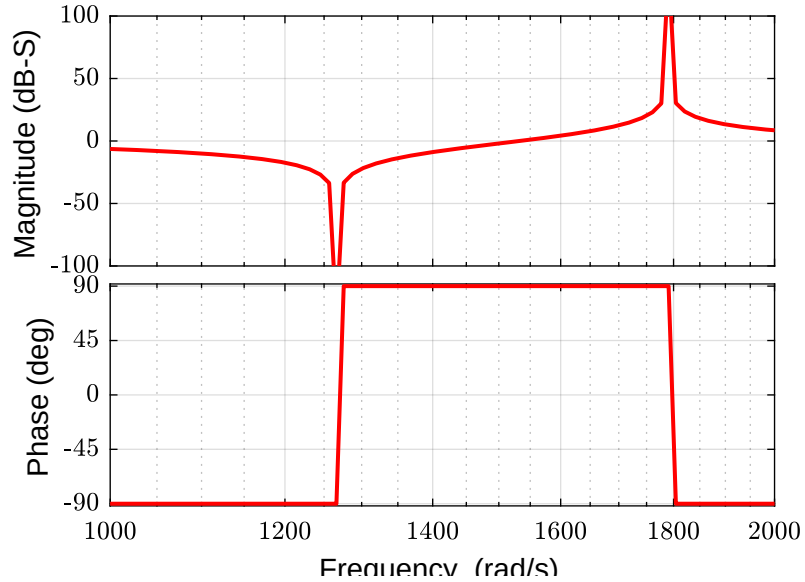

(a)

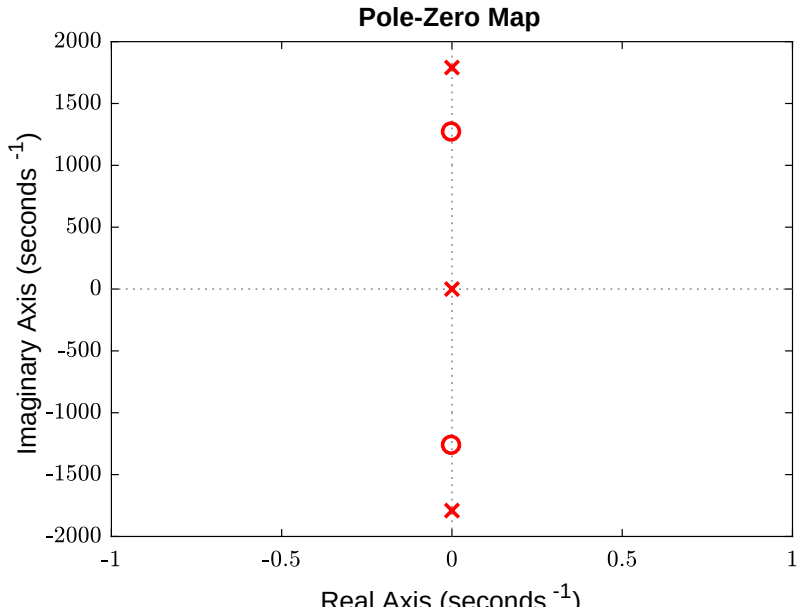

(b)

Figure 4.2: LCL Filter: (a) Frequency response of the LCL filter transfer function (4.1); (b) pole-zero plot of the LCL filter transfer function (4.1).

The peaks produced by resonant frequency ω_p and anti-resonant frequency ω_z are shown in Fig. 4.2(a). The harmonics appearing in these region will be greatly amplified. The poles and zeros of the transfer function (4.1) are shown in Fig. 4.2(b). It can be seen in the figure that poles and zeros of the transfer function appear on

the imaginary axis of the $s-$plane, which can make the system unstable.

4.1 Passive damping

The introduction of resistor (R_d) in series with the filter capacitor C_f and in parallel with the grid-side filter inductor L_{fg} can bring the two unstable poles (4.2(b)) of the LCL filter based system in the stable region. The topology for passive damping is shown in Fig. 4.3.

The transfer function from $\boldsymbol{u}_{\mathrm{c}}^{\mathrm{s}}(s)$ to $\boldsymbol{i}_{\mathrm{c}}^{\mathrm{s}}(s)$ with the damping resistor R_d connected in series with the filter capacitor C_f is:

$$\frac{\boldsymbol{i}_{\mathrm{c}}^{\mathrm{s}}(s)}{\boldsymbol{u}_{\mathrm{c}}^{\mathrm{s}}(s)} = \frac{1}{L_{fc}} \frac{s^2 \frac{R_d}{L_{fg}} s + \frac{1}{L_{fg} C_f}}{s(s^2 + \frac{(L_{fc}+L_{fg})}{Lfc} \frac{R_d}{L_{fg}} s + \frac{L_{fg}+L_{fc}}{L_{fg} L_{fc} C_f})} \tag{4.2}$$

The transfer function from $\boldsymbol{u}_{\mathrm{c}}^{\mathrm{s}}(s)$ to $\boldsymbol{i}_{\mathrm{c}}^{\mathrm{s}}(s)$ with damping resistor R_d connected in parallel with the grid side inductor L_{fg} is:

$$\frac{\boldsymbol{i}_{\mathrm{c}}^{\mathrm{s}}(s)}{\boldsymbol{u}_{\mathrm{c}}^{\mathrm{s}}(s)} = \frac{1}{L_{fc}} \frac{s^2 + \frac{1}{C_f R_d} s + \frac{1}{L_{fg} C_f}}{s(s^2 + \frac{1}{C_f R_d} s + \frac{L_{fg}+L_{fc}}{L_{fg} L_{fc} C_f})} \tag{4.3}$$

The effect of adding damping resistor to the LCL filter can be seen in Fig. 4.4. The figure clearly shows the decrease in the resonant peak and the absence of zero-crossing phase.

Though passive damping is a reliable method for damping LCL filter resonance, it comes with a cost of sustainable power loss. Harmonic losses decreases with the increase in damping resistor value, but at the same time it decreases the effectiveness of the filter. Introducing resistor will generate heat and reduce the overall efficiency of the system and will demand additional cooling. This will also increase the size and cost of the filter.

4.2 Active damping

The converter current $\boldsymbol{i}_{\mathrm{c}}^{\mathrm{s}}$ is used as feedback for the current controller, as a result of which the switching-induced harmonics which appears in the waveforms of $\boldsymbol{i}_{\mathrm{c}}^{\mathrm{s}}$ are amplified to the grid current $\boldsymbol{i}_{\mathrm{g}}^{\mathrm{s}}$ due to the filter resonance ω_z. A reduced order model is used for resonance damping of filter resonance ω_z, where converter current $\boldsymbol{i}_{\mathrm{c}}^{\mathrm{s}}$ is considered as input and grid current $\boldsymbol{i}_{\mathrm{g}}^{\mathrm{s}}$ is considered as output.

The transfer function from $\boldsymbol{i}_{\mathrm{c}}^{\mathrm{s}}(s)$ to $\boldsymbol{i}_{\mathrm{g}}^{\mathrm{s}}(s)$ is

$$\frac{\boldsymbol{i}_{\mathrm{g}}^{\mathrm{s}}(s)}{\boldsymbol{i}_{\mathrm{c}}^{\mathrm{s}}(s)} = \frac{1}{L_{fg} C_f s^2 + 1} \tag{4.4}$$

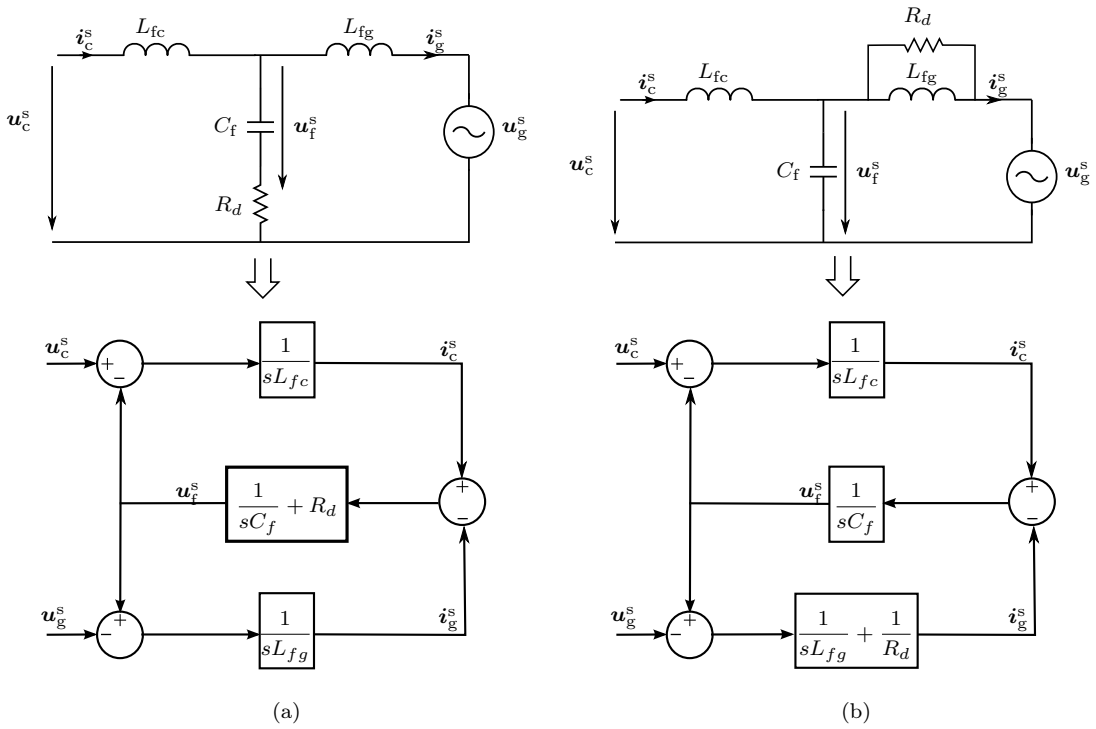

Figure 4.3: Block diagram for equivalent circuit of LCL filter: (a) passive damping with resistor in series with the capacitor and (b) in parallel with the grid side filter inductor [13].

The frequency response of the transfer function is shown in Fig. 4.6(a). The resonance between the converter and grid current occurring at frequency ω_z can be clearly seen in the figure. Therefore, this is the frequency which requires damping.

An active damping strategy based upon the concept of virtual resistor (VR) is applied to damp the resonance occurring at frequency ω_z [2,24]. VR concept is based upon emulating the effect of physical resistor by changing the converter reference with an additional damping component.

An LCL filter which consists of a resistor R_v connected in parallel to the filter capacitor C_f is represented by the s-domain block diagram shown in Fig. 4.5. The damping effect of R_v can be realized by adding the component $-\boldsymbol{u}_{\mathrm{f}}^{\mathrm{s}}/R_v$ to the converter current $\boldsymbol{i}_{\mathrm{c}}^{\mathrm{s}}$. The modified transfer function from $\boldsymbol{i}_{\mathrm{c}}^{\mathrm{s}}(s)$ to $\boldsymbol{i}_{\mathrm{g}}^{\mathrm{s}}(s)$ is

$$\frac{\boldsymbol{i}_{\mathrm{g}}^{\mathrm{s}}(s)}{\boldsymbol{i}_{\mathrm{c}}^{\mathrm{s}}(s)} = \frac{s^2 + 1/(L_{fg}C_f)}{(L_{fg}C_f s^2 + 1)(R_v C_f L_{fg} s^2 + L_{fg} s + R_v)} \tag{4.5}$$

The frequency repose for the modified transfer function is showing Fig. 4.6(a). The virtual resistance R_v is obtained by comparing the poles of the transfer function (4.5) to the poles of a second order polynomial.

$$R_v = \frac{1}{2\zeta_{ad}} \sqrt{\frac{L_{fg}}{C_f}} \tag{4.6}$$

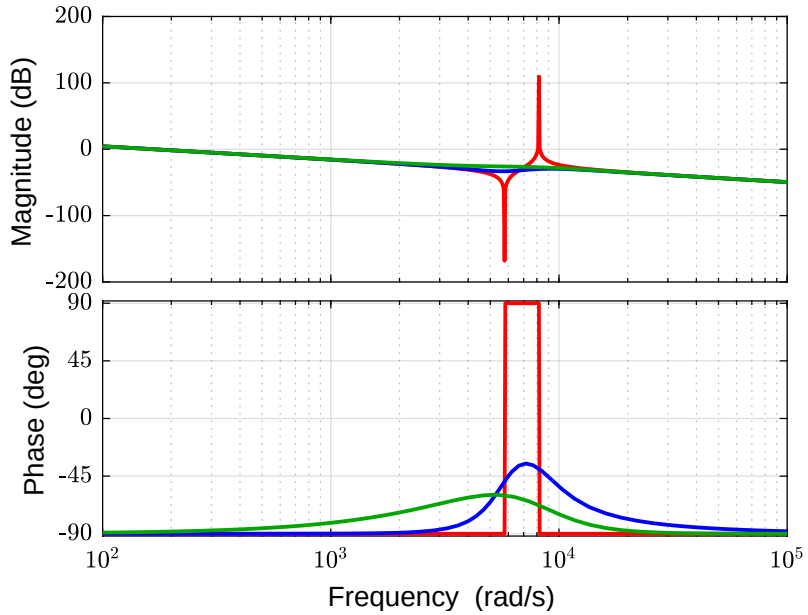

Figure 4.4: Passive damping: Damping resistor R_d connected in series with the filter capacitor C_f is represented by the blue line and R_d connected in parallel to the grid-side filter L_{fg} inductor is represented by the green line. Red line represents the undamped frequency response of LCL filter.

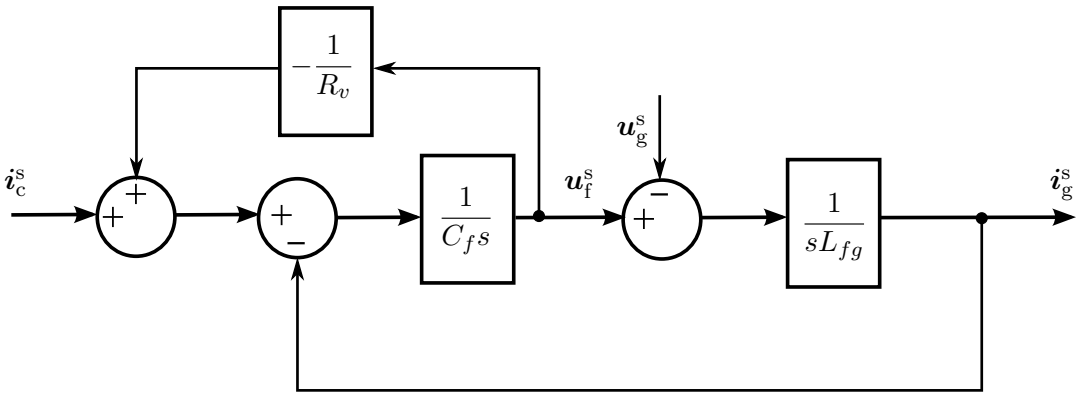

Figure 4.5: s-domain block representation of LCL-filter with a damping resistor R_v in parallel with the filter capacitor.

where ζ_{ad} is the damping ratio. The damping ratio $\zeta_{ad} = 1$ is selected to damp the resonance frequency ω_z.

The emulation based damping is used in this thesis to damp the resonance occurring at frequency ω_z. Active damping is implemented in dq coordinates and the signal-flow diagram is shown in Fig. 4.7. The fundamental voltage waveform of the capacitor voltage $\boldsymbol{u}_{\mathrm{f}}$ will cause power flow disturbance. Therefore, the fundamental voltage waveform of the capacitor voltage $\boldsymbol{u}_{\mathrm{f}}$ is extracted by passing it through a

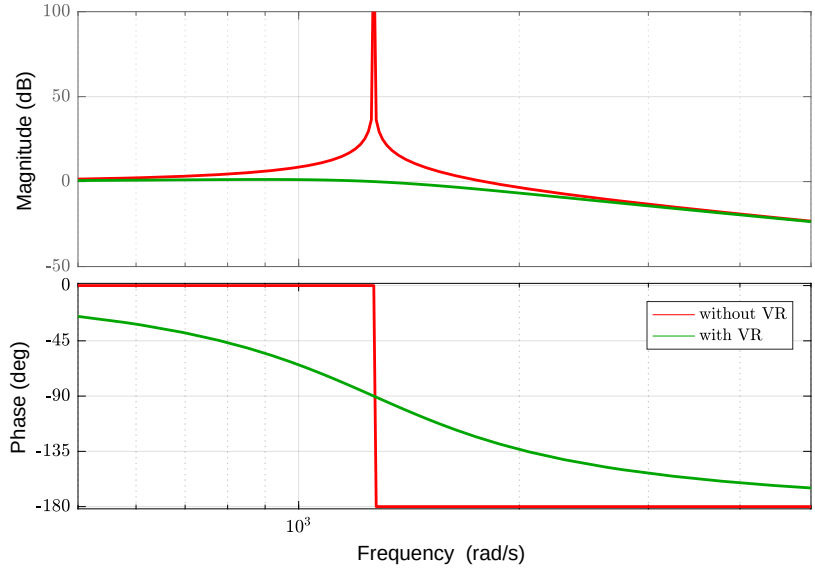

(a)

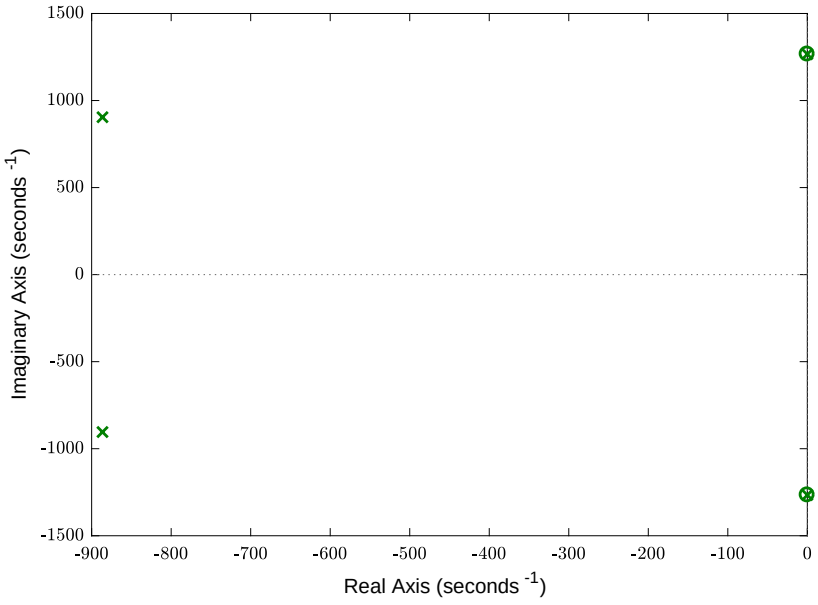

(b)

Figure 4.6: Active damping: (a) Red line represents frequency response of the LCL filter without virtual resistance and the green line represents the frequency response of LCL filter in the presence of a virtual resistance; (b) pole-zero plot of the transfer function (4.5).

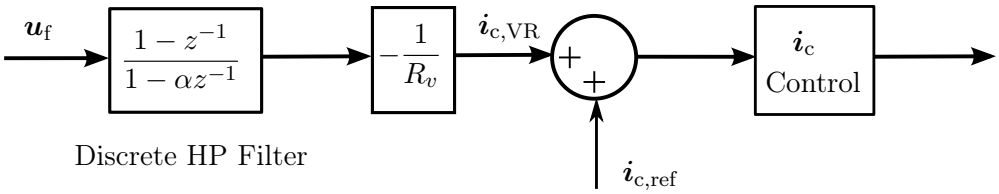

Figure 4.7: Signal flow graph for active damping [9].

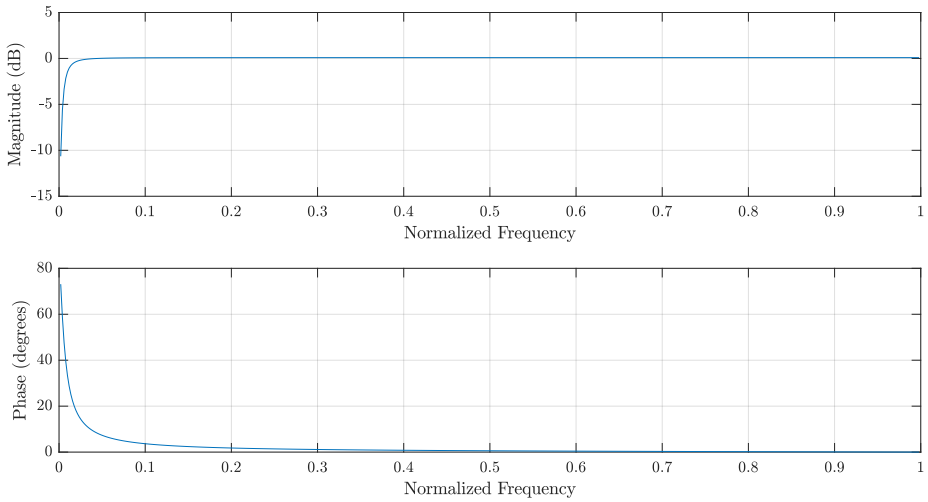

Figure 4.8: Frequency response of the discrete HP filter used in active damping of LCL resonance.

digital high pass (HP) filter.

The virtual resistor active damping is emulated by adding the quantity

$$\boldsymbol{i}_\mathrm{c,VR} = -\frac{\boldsymbol{u}_\mathrm{f,filtered}}{R_v}$$

to the converter reference current $\boldsymbol{i}_\mathrm{c,ref}$, where $\boldsymbol{u}_\mathrm{f,filtered}$ is the capacitor voltage $\boldsymbol{u}_\mathrm{f}$ filtered using a digital HP filter. The transfer function for high pass discrete filter is obtained by using the discrete filter tool available in MATLAB. The frequency response of the discrete HP filter is shown in Fig. 4.8.

5 State Observer

The implementation of the designed current controller requires the measurement of the state elements ($\boldsymbol{i}_\mathrm{c}$, $\boldsymbol{u}_\mathrm{f}$ and $\boldsymbol{i}_\mathrm{g}$) of the LCL filter and the grid voltage $\boldsymbol{u}_\mathrm{g}$. These measurements can be accomplished using expensive high precesion sensors. The expense of the controller can be decreased by estimating the state elements using an observer rather than measuring them. It also provides smoothed values of the measurements, which may be contaminated by noise [25].

5.1 Observability

An observer can be used to measure the states of the system, if the system is observable. The observability matrix is given by

$$\mathbf{W}_o = \begin{bmatrix} \mathbf{C}_\mathrm{c} \\ \mathbf{C}_\mathrm{c}\mathbf{\Phi} \\ \vdots \\ \mathbf{C}_\mathrm{c}\mathbf{\Phi}^{n-1} \end{bmatrix}$$

where n is the order of the system matrix $\mathbf{\Phi}$. The system is observable, if the matrix $\mathbf{W}_o$ has full rank. The observability matrix $\mathbf{W}_o$ for the parameters given in Table. 6.1 has a full rank of three. Therefore, all the states of the system are observable and an observer can be designed to estimate the state elements.

5.2 Observer design

The block diagram explaining the integration of observer in the control scheme of FS-MPC is shown in Fig.5.1. The state observer gives the estimate of capacitor voltage $\boldsymbol{u}_\mathrm{f}$ and grid current $\boldsymbol{i}_\mathrm{g}$ based upon the present control signal (converter voltage $\boldsymbol{u}_\mathrm{c}$) and output (converter current $\boldsymbol{i}_\mathrm{c}$).

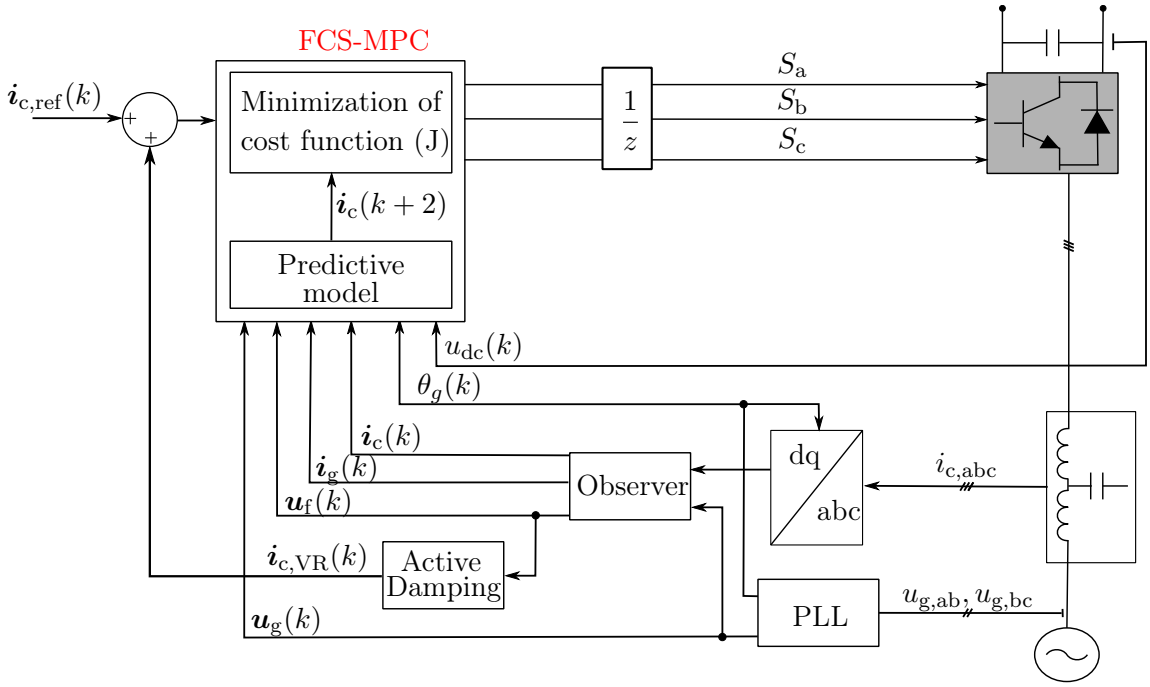

Figure 5.1: Block diagram for the control scheme including observer and active resonance damping.

The state observer is given by

$$\begin{aligned}\hat{\mathbf{x}}(k+1) &= \boldsymbol{\Phi}\hat{\mathbf{x}}(k) + \boldsymbol{\Gamma}_{\mathrm{c}}\boldsymbol{u}_{\mathrm{c}}(k) + \boldsymbol{\Gamma}_{\mathrm{g}}\boldsymbol{u}_{\mathrm{g}}(k) + \mathbf{K_o}[\boldsymbol{i}_{\mathrm{c}}(k) - \mathbf{C}_{\mathrm{c}}\hat{\mathbf{x}}(k)] \\ &= [\boldsymbol{\Phi} - \mathbf{K_o}\mathbf{C}_{\mathrm{c}}]\hat{\mathbf{x}}(k) + \boldsymbol{\Gamma}_{\mathrm{c}}\boldsymbol{u}_{\mathrm{c}}(k) + \boldsymbol{\Gamma}_{\mathrm{g}}\boldsymbol{u}_{\mathrm{g}}(k) + \mathbf{K_o}\boldsymbol{i}_{\mathrm{c}}(k)\end{aligned} \tag{5.1}$$

where $\mathbf{K_o} = [k_{o1}\ k_{o2}\ k_{o3}]^{\mathrm{T}}$ is the observer gain matrix.

The characteristic equation for the estimation error dynamics is

$$\begin{aligned}\boldsymbol{a}_{\mathrm{o}}(z) =& \det(z\mathbf{I} - \boldsymbol{\Phi} + \mathbf{K_o}\mathbf{C}_{\mathrm{c}}) \\ =& z^3 + (k_{o1} - a_{22} - a_{33} - a_{11})z^2 + (a_{11}a_{22} - a_{12}a_{21} + a_{11}a_{33} - a_{13}a_{31} \\ &+ a_{22}a_{33} - a_{23}a_{32} + a_{12}k_{o2} + a_{13}k_{o3} - a_{22}k_{o1} - a_{33}k_{o1})z - a_{11}a_{22}a_{33} \\ &+ a_{11}a_{23}a_{32} + a_{12}a_{21}a_{33} - a_{12}a_{23}a_{31} - a_{13}a_{21}a_{32} + a_{13}a_{22}a_{31} + a_{12}a_{23}k_{o3} \\ &- a_{13}a_{22}k_{o3} - a_{12}a_{33}k_{o2} + a_{13}a_{32}k_{o2} + a_{22}a_{33}k_{o1} - a_{23}a_{32}k_{o1}\end{aligned} \tag{5.2}$$

The desired characteristic polynomial is

$$\begin{aligned}\boldsymbol{a}_{\mathrm{o}}(z) =& (z - \boldsymbol{\alpha}_{01})(z - \boldsymbol{\alpha}_{02}))(z - \boldsymbol{\alpha}_{03}) \\ =& z^3 + (-\boldsymbol{\alpha}_{01} - \boldsymbol{\alpha}_{02} - \boldsymbol{\alpha}_{03})z^2 + (\boldsymbol{\alpha}_{01}\boldsymbol{\alpha}_{02} + \boldsymbol{\alpha}_{01}\boldsymbol{\alpha}_{03} + \boldsymbol{\alpha}_{02}\boldsymbol{\alpha}_{03})z - \boldsymbol{\alpha}_{01}\boldsymbol{\alpha}_{02}\boldsymbol{\alpha}_{03}\end{aligned} \tag{5.3}$$

The poles of $\boldsymbol{a}_{\mathrm{o}}(z)$ can be mapped using the poles of its continuous-time counterpart $(s+\alpha_{od})(s+\zeta_{or}\omega_{or} \pm j\omega_{or}\sqrt{1-\zeta_{or}^2})$. The poles obtained from continuous-time

domain can be mapped into discrete-time domain via $z = e^{sT_s}$, where T_s is the sample time and s represents the poles of the continuous-time transfer function. The observer poles should be placed such that they are twice as fast as the controller dynamics [1]. The real pole α_{od} determines the dominant dynamics of the system and the complex-conjugate poles (parametrized via ω_{or} and ζ_{or}) determines the overshoot and settling time of the system. The bandwidth of the current controller is calculated analytically and the dominant pole α_{od} of the observer is set to twice the bandwidth of the predictive controller α_{pc}. The parameter ω_{or} is kept at the resonant frequency $\omega_p - \omega_g$ and the damping ratio ζ_{or} is set to 0.7. The observer parameters are shown in Table. 6.2.

By using equation (5.2) and (5.3), the observer gain matrix $\mathbf{K_o}$ is obtained. The closed-form expression of observer gain matrix $\mathbf{K_o}$ is given in [1].

5.3 Disturbance estimation

The disturbance signal in the observer can be estimated and used to reject the constant disturbance present in the predicted converter current $\boldsymbol{i}_\mathrm{c}$. The state-space equation (2.12) governing the continuous-time dynamics of the converter current is modified to take the disturbance w into account

$$\begin{aligned}
\frac{d}{dt}\underbrace{\begin{bmatrix}\boldsymbol{i}_\mathrm{c}\\ \boldsymbol{u}_\mathrm{f}\\ \boldsymbol{i}_\mathrm{g}\end{bmatrix}}_{\mathbf{x}} &= \underbrace{\begin{bmatrix}-j\omega_g & -\frac{1}{L_{fc}} & 0\\ \frac{1}{C_f} & -j\omega_g & -\frac{1}{C_f}\\ 0 & \frac{1}{L_{fg}} & -j\omega_g\end{bmatrix}}_{\mathbf{A}}\begin{bmatrix}\boldsymbol{i}_\mathrm{c}\\ \boldsymbol{u}_\mathrm{f}\\ \boldsymbol{i}_\mathrm{g}\end{bmatrix} + \underbrace{\begin{bmatrix}\frac{1}{L_{fc}}\\ 0\\ 0\end{bmatrix}}_{\mathbf{B}_\mathrm{c}}\boldsymbol{u}_\mathrm{c} + \underbrace{\begin{bmatrix}0\\ 0\\ -\frac{1}{L_{fg}}\end{bmatrix}}_{\mathbf{B}_\mathrm{g}}\boldsymbol{u}_\mathrm{g} + \underbrace{\begin{bmatrix}1\\ 0\\ 0\end{bmatrix}}_{\mathbf{B}_\mathrm{w}} w\\
\boldsymbol{i}_\mathrm{c} &= \underbrace{\begin{bmatrix}1 & 0 & 0\end{bmatrix}}_{\mathbf{C}_\mathrm{c}}\mathbf{x}
\end{aligned} \tag{5.4}$$

Accordingly, the discrete-time model (2.15) is modified to include the disturbance w in the converter current dynamics.

$$\begin{aligned}
\mathbf{x}(k+1) &= \mathbf{\Phi}\mathbf{x}(k) + \mathbf{\Gamma}_\mathrm{c}\boldsymbol{u}_\mathrm{c}(k) + \mathbf{\Gamma}_\mathrm{g}\boldsymbol{u}_\mathrm{g}(k) + \mathbf{\Gamma}_\mathrm{w}w(k)\\
\boldsymbol{i}_\mathrm{c}(k) &= \mathbf{C}_\mathrm{c}\mathbf{x}(k)
\end{aligned} \tag{5.5}$$

$$\mathbf{\Gamma}_\mathrm{w} = \left(\int_0^{T_s} \mathrm{e}^{\mathbf{A}\tau}d\tau\right)\mathbf{B}_\mathrm{w} = \boldsymbol{\gamma}\begin{bmatrix}\dfrac{L_{fg}\sin(T_s\omega_p) + L_{fc}T_s w_p}{(L_{fg}+L_{fc})w_p}\\ \dfrac{2L_{fc}L_{fg}\sin(T_s w_p/2)^2}{L_{fg}+L_{fc}}\\ \dfrac{2L_{fc}(T_s/2 - \sin(T_s w_p)/(2w_p))}{L_{fg}+L_{fc}}\end{bmatrix} \tag{5.6}$$

For disturbance rejection, the system model (2.15) is augmented with a disturbance state resulting in

$$\underbrace{\begin{bmatrix}\mathbf{x}(k+1)\\ \mathbf{w}(k+1)\end{bmatrix}}_{\mathbf{x}_w} = \underbrace{\begin{bmatrix}\mathbf{\Phi} & \mathbf{\Gamma}_{\mathrm{w}}\\ 0 & 1\end{bmatrix}}_{\mathbf{\Phi}_w}\begin{bmatrix}\mathbf{x}(k)\\ \mathbf{w}(k)\end{bmatrix} + \underbrace{\begin{bmatrix}\mathbf{\Gamma}_{\mathrm{c}}\\ 0\end{bmatrix}}_{\mathbf{\Gamma}_{\mathrm{cw}}}\boldsymbol{u}_{\mathrm{c}}(k) + \underbrace{\begin{bmatrix}\mathbf{\Gamma}_{\mathrm{g}}\\ 0\end{bmatrix}}_{\mathbf{\Gamma}_{\mathrm{gw}}}\boldsymbol{u}_{\mathrm{g}}(k)$$
$$\boldsymbol{i}_{\mathrm{c}}(k) = \underbrace{[\mathbf{C}_{\mathrm{c}}\ 0]}_{\mathbf{C}_{\mathrm{cw}}}\mathbf{x}_w(k) \tag{5.7}$$

where $\mathbf{x}_w$ is the augmented state vector; and $\mathbf{\Phi}_w$, $\mathbf{\Gamma}_{\mathrm{cw}}$ and $\mathbf{\Gamma}_{\mathrm{gw}}$ are the augmented system matrices. From (2.15) and (5.7), the state observer becomes

$$\begin{aligned}\hat{\mathbf{x}_w}(k+1) &= \mathbf{\Phi}_w\hat{\mathbf{x}}(k) + \mathbf{\Gamma}_{\mathrm{cw}}\boldsymbol{u}_{\mathrm{c}}(k) + \mathbf{\Gamma}_{\mathrm{gw}}\boldsymbol{u}_{\mathrm{g}}(k) + \mathbf{K_{ow}}[\boldsymbol{i}_{\mathrm{c}}(k) - \mathbf{C}_{\mathrm{cw}}\hat{\mathbf{x}}(k)] \\ &= [\mathbf{\Phi}_w - \mathbf{K_{ow}}\mathbf{C}_{\mathrm{cw}}]\hat{\mathbf{x}_w}(k) + \mathbf{\Gamma}_{\mathrm{cw}}\boldsymbol{u}_{\mathrm{c}}(k) + \mathbf{\Gamma}_{\mathrm{gw}}\boldsymbol{u}_{\mathrm{g}}(k) + \mathbf{K_{ow}}\boldsymbol{i}_{\mathrm{c}}(k)\end{aligned} \tag{5.8}$$

where $\mathbf{K_{ow}} = [\mathbf{k}_{ow1}\ \mathbf{k}_{ow2}\ \mathbf{k}_{ow3}\ \mathbf{k}_{ow4}]^{\mathrm{T}}$ is the observer gain matrix. The characteristic equation of the estimation error dynamic is

$$\boldsymbol{a}_{\mathrm{ow}}(z) = det(z\mathbf{I} - \mathbf{\Phi}_w + \mathbf{K_{ow}}\mathbf{C}_{\mathrm{cw}}) \tag{5.9}$$

The desired characteristic polynomial is

$$\boldsymbol{a}_{\mathrm{o}}(z) = (z - \boldsymbol{\alpha}_{01})(z - \boldsymbol{\alpha}_{02}))(z - \boldsymbol{\alpha}_{03})(z - \boldsymbol{\alpha}_{04}) \tag{5.10}$$

In the characteristic polynomial (5.10), the two complex poles $\boldsymbol{\alpha}_{01,02}$ are placed to determine the dominant dynamics and the other two poles $\boldsymbol{\alpha}_{03,04}$ are placed at high frequency to keep the observer stable and fast. The poles of $\boldsymbol{a}_{\mathrm{ow}}(z)$ is first placed in continuous-time domain and then mapped to discrete-time domain using $z = e^{sTs}$. The continuous-time pole is split into two second-order polynomial

$$(s + \zeta_{orw}\omega_{orw} \pm j\omega_{orw}\sqrt{1-\zeta_{orw}^2})(s + \zeta_{odw}\omega_{odw} \pm j\omega_{odw}\sqrt{1-\zeta_{odw}^2}) \tag{5.11}$$

As stated previously, the poles of the observer should be placed such that it is atleast twice as fast as the controller. so ω_{orw} is placed at $2\alpha_{pc}$, ω_{odw} is placed at the resonant frequency $\omega_p - \omega_g$. The damping ratio $\zeta_{orw} = 0.7$ and $\zeta_{odw} = 0.5$ is selected. The corresponding discrete-time poles are

$$\boldsymbol{\alpha}_{01,02} = \exp[(-\zeta_{orw}\omega_{orw} \pm j\omega_{orw}\sqrt{1-\zeta_{orw}^2})T_s] \tag{5.12}$$

$$\boldsymbol{\alpha}_{01,02} = \exp[(-\zeta_{odw}\omega_{odw} \pm j\omega_{odw}\sqrt{1-\zeta_{odw}^2})T_s] \tag{5.13}$$

By using equation (5.9) and (5.10), the observer gain matrix $\mathbf{K_{ow}}$ is obtained.

6 Results

The results of this thesis are based upon simulations performed using MATLAB and Simulink.

6.1 Simulations

The simulation model based on current trajectory and optimal control are shown in Fig.6.1 and Fig. 6.2 respectively. The filter and controller parameters used in simulation are given in Table 6.1 and Table 6.2 respectively. The "Converter and LCL filter" subsystem is based upon the continuous time model of LCL filter given in Chapter 2 and the "Predictive control" subsystem inside the purple box is based upon the FS model predictive current control given in chapter 3.

Table 6.1: Parameter of LCL filter used in simulations.

DC-link voltage	u_{dc}	5 kV
Grid line-line voltage	U_{LL}	3 kV
Converter-side inductance	L_{fc}	0.567 mH
Grid-side inductance	L_{fg}	0.567 mH
Capacitance	C_f	1.1 mF

Table 6.2: Parameter of controller and observer used in simulations.

Bandwidth	α_{od}	$2\pi(345)$ rad/s
Natural frequency	ω_{or}	$\omega_p - \omega_g$
	ω_{od}	$2\pi.345$ rad/s
Damping ratio	ζ_{or}	0.7
	ζ_{od}	0.5
Sampling frequency	f_s	6 kHz

Simulations are performed at a sampling frequency f_{sw} of 6 kHz, so as to maintain a low switching frequency which is suitable for low voltage applications. An average switching frequency of 982 kHz was achieved as shown in Fig. 6.4 with a THD of 4.04% for grid-side current as shown in Fig. 6.3. It can be seen from the figure that the resonance occurring at resonant frequency $\omega_z = 1266.3$ rad/s is successfully damped. The switching frequency at each sampling instant corresponding to each leg of the converter are shown in Fig. 6.5. It can be seen from the figure that the highest switching frequency is 3 kHz and the lowest switching frequency is 0 kHz, where 0 kHz means that the switching state applied in the previous time instant was kept constant. The switching state corresponding to each leg of the converter are shown in Fig. 6.6. The three-phase converter-side current with high THD and the filtered three-phase grid-side current with low THD are shown in Fig. 6.7 and Fig. 6.8 respectively. The current controller is implemented in dq coordinates and the converter current $\boldsymbol{i}_{\mathrm{c}}$ is used as feedback. In order to produce desired grid current $\boldsymbol{i}_{\mathrm{g}}$ at PCC, the converter reference current $\boldsymbol{i}_{\mathrm{c,ref}}$ is calculated using equation (3.16). Grid current $\boldsymbol{i}_{\mathrm{g}}$ tracking for d-axis and q-axis are shown in Fig. 6.9. The presence of steady-state error and coupling of the d & q axis can be clearly seen in the figure. The real power p_g and reactive power q_g at PCC is shown in Fig. 6.10.

Observer was implemented to estimate the state of the system. Fig. 6.11, Fig. 6.12 and Fig. 6.13 shows the performance of the observer in estimating the state elements $\boldsymbol{i}_{\mathrm{c}}$, $\boldsymbol{i}_{\mathrm{g}}$ and $\boldsymbol{u}_{\mathrm{f}}$. It can be seen from the figure that the estimation error between measured and estimated values of the state elements are negligible.

6.2 Parameter sensitivity

Manufacturing tolerance of 10% is considered for the filter components. The robustness of the current controller against parameter variation is analyzed by increasing the filter parameters for controller by 10% and the filter parameters for plant model was kept at nominal value. The system remained stable for the examined range. Fig. 6.14 demonstrates the robustness of the controller against parameter errors.

6.3 Performance comparison

The performance of the FS model predictive current controller is compared with an observer based state-space controller at low switching frequency. The THD of the grid current $\boldsymbol{i}_{\mathrm{g}}$ at a switching frequency of 1 kHz is 4.15%. The simulated three-phase grid current and spectrum of grid current for state-space controller is shown in Fig. 6.15 and Fig. 6.16 respectively. The THD of grid current for FS model predictive current controller at a switching frequency of 982 kHz is 4.04% (Fig. 6.3). Therefore, the performance of FS model predictive current controller is better than observer based state-space controller at low switching frequency. The performance of the state-space controller at low switching frequency can be improved by optimizing the pulse-width-modulation method used in the controller.

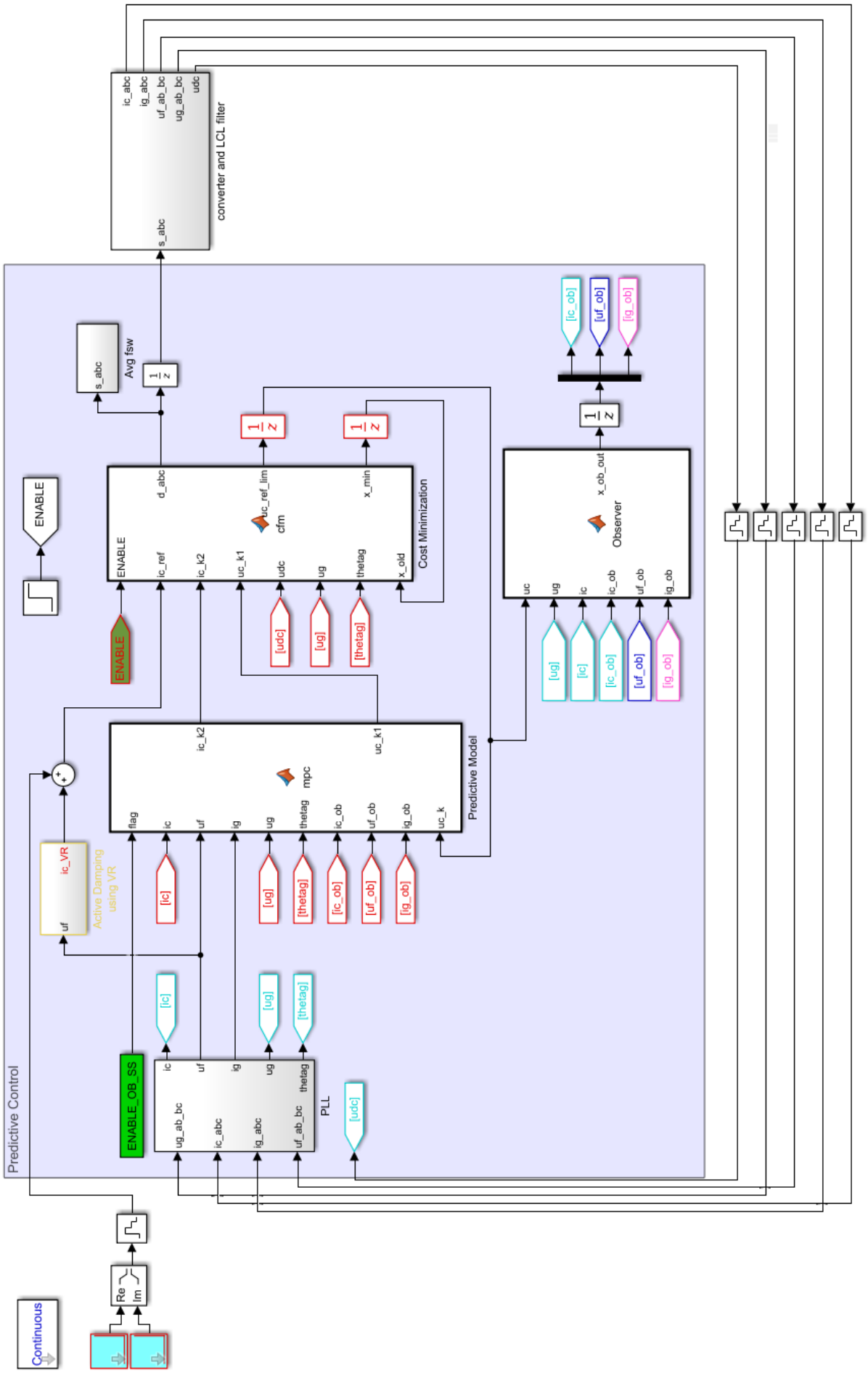

Figure 6.1: Simulation model of a grid connected converted equipped with an LCL filter based upon current trajectory.

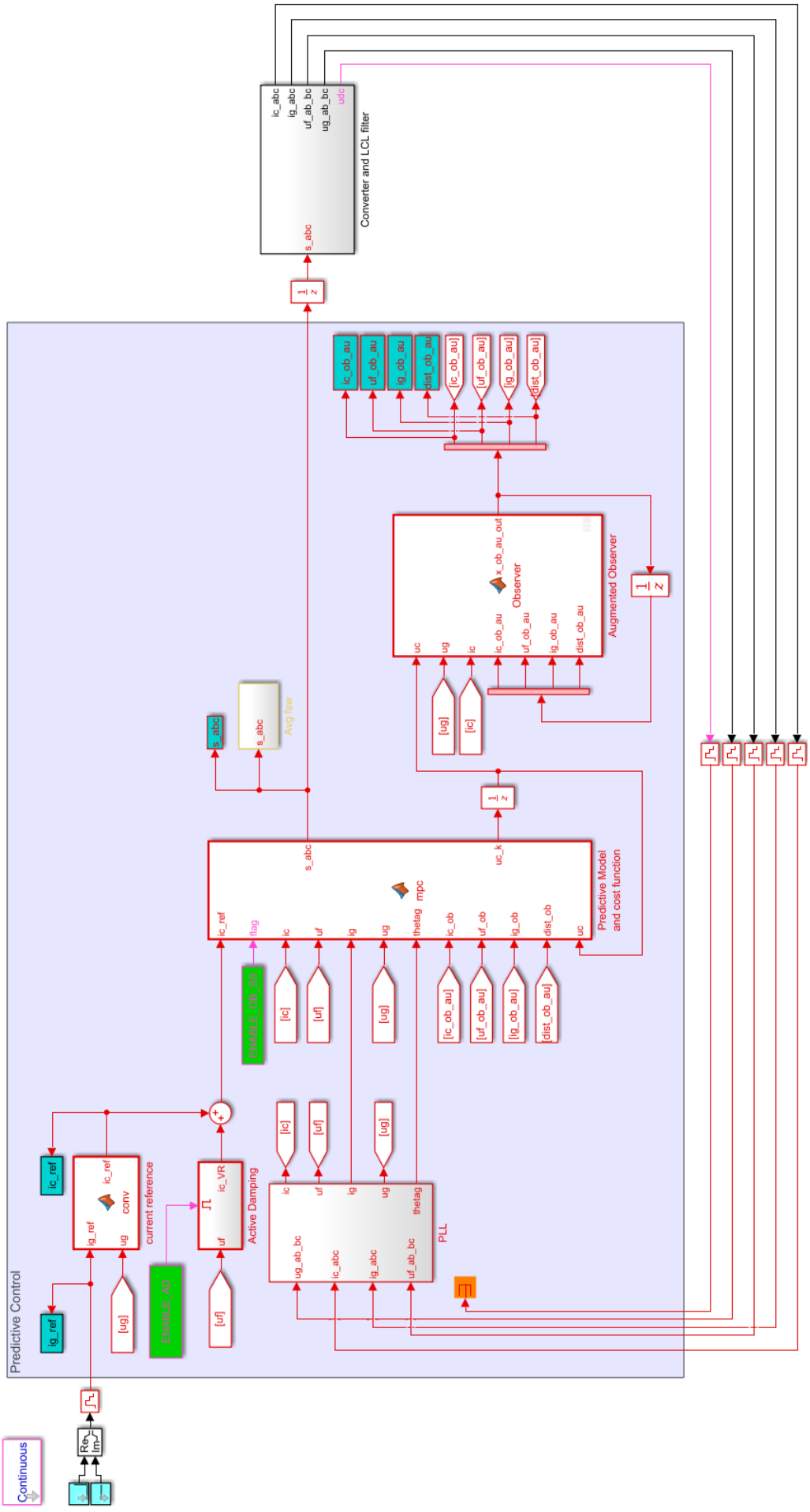

Figure 6.2: Simulation model of a grid connected converted equipped with an LCL filter based upon optimal control.

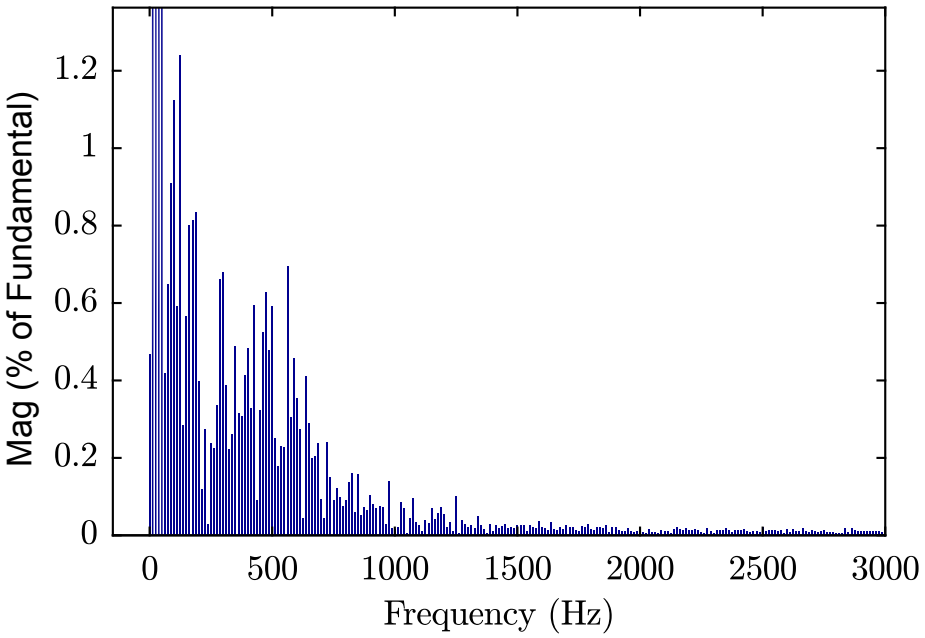

Figure 6.3: Simulation results showing grid current spectrum. The THD of grid current is 4.04% and fundamental (50 Hz) = 1.8 kA .

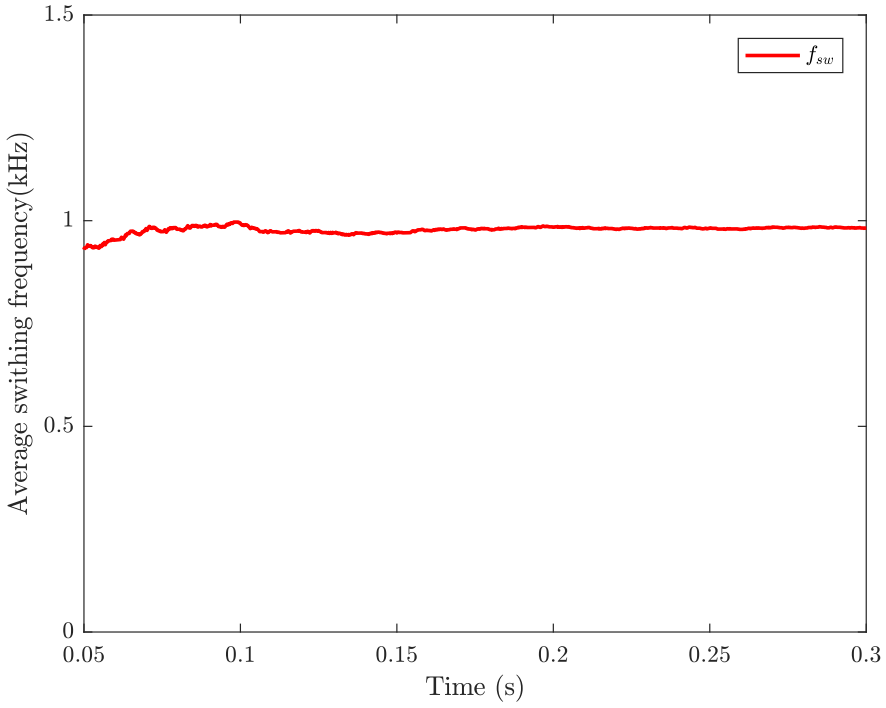

Figure 6.4: Simulation results showing sampled values of average switching frequency when the sampling frequency f_{sw} is 6kHz. An average switching frequency of 982 Hz is achieved.

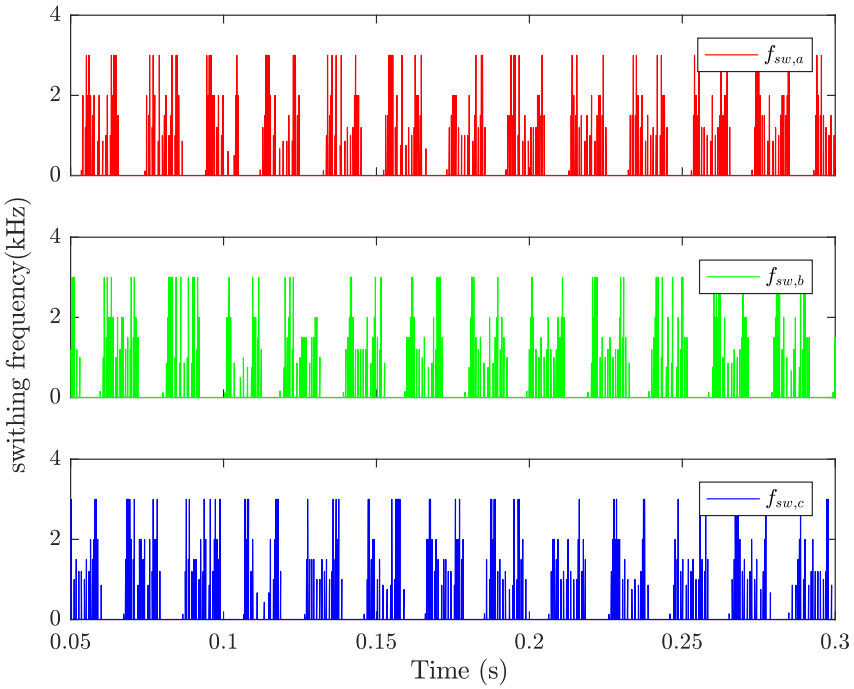

Figure 6.5: Simulation results showing sampled values of switching frequency corresponding to leg a (red), leg b (green) and leg c (blue) of the converter.

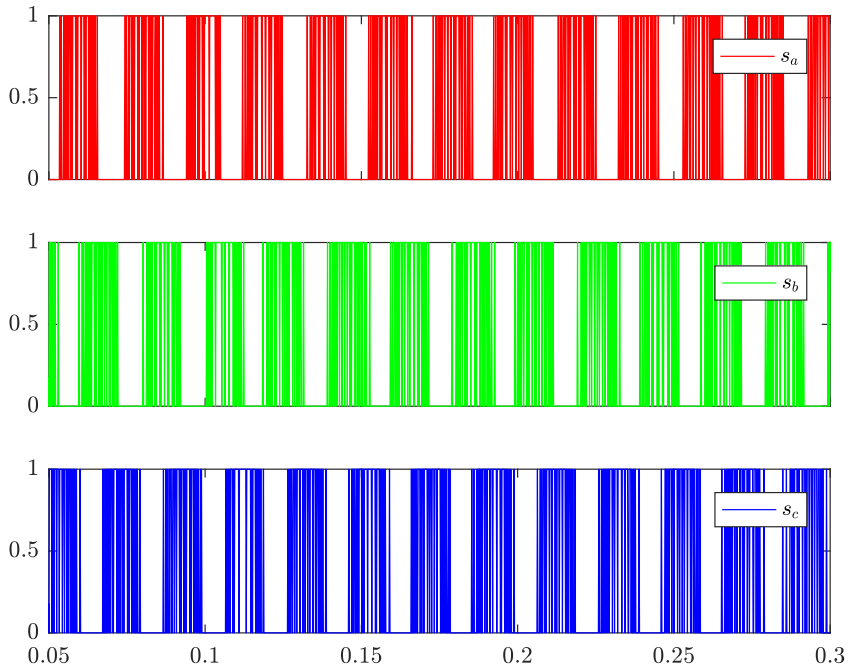

Figure 6.6: Simulation results showing sampled values of switching states corresponding to leg a (red), leg b (green) and leg c (blue) of the converter.

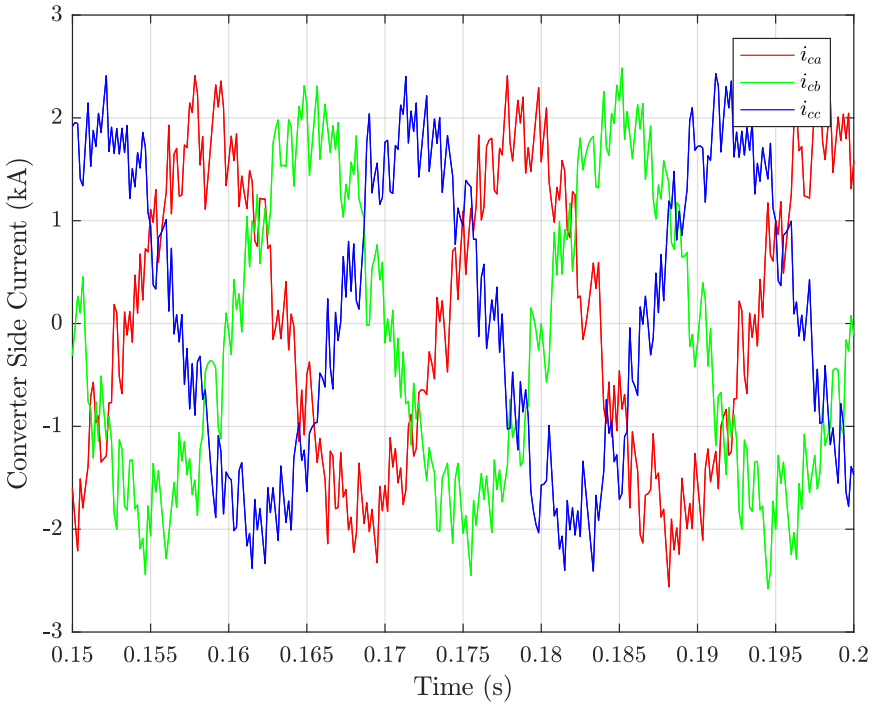

Figure 6.7: Simulation results showing sampled values of three-phase converter current: i_{ca} (red), i_{cb} (green) and i_{cc} (blue).

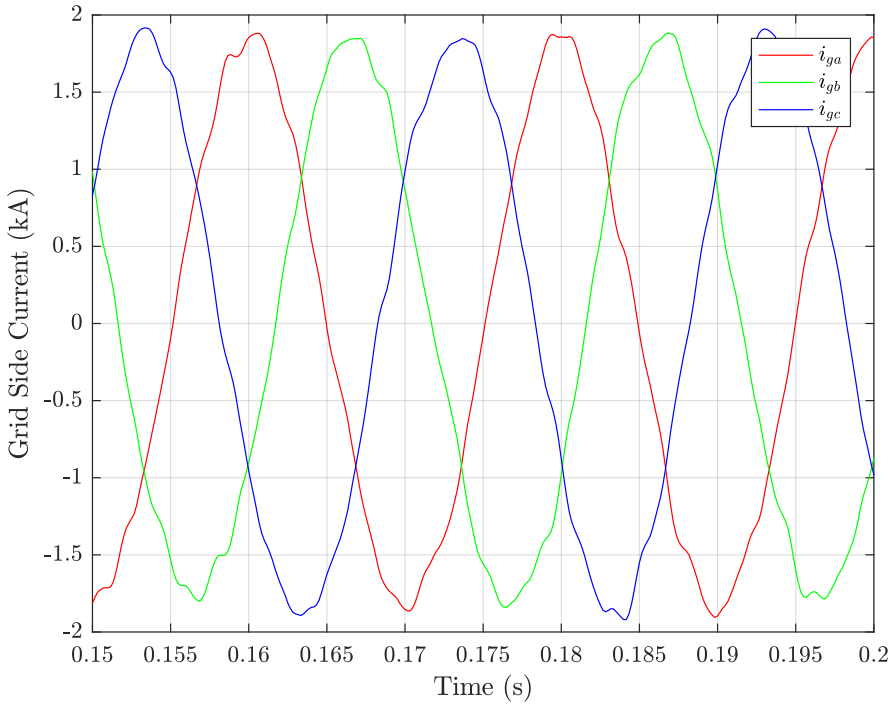

Figure 6.8: Simulation results showing sampled values of three-phase grid current: i_{ca} (red), i_{cb} (green) and i_{cc} (blue).

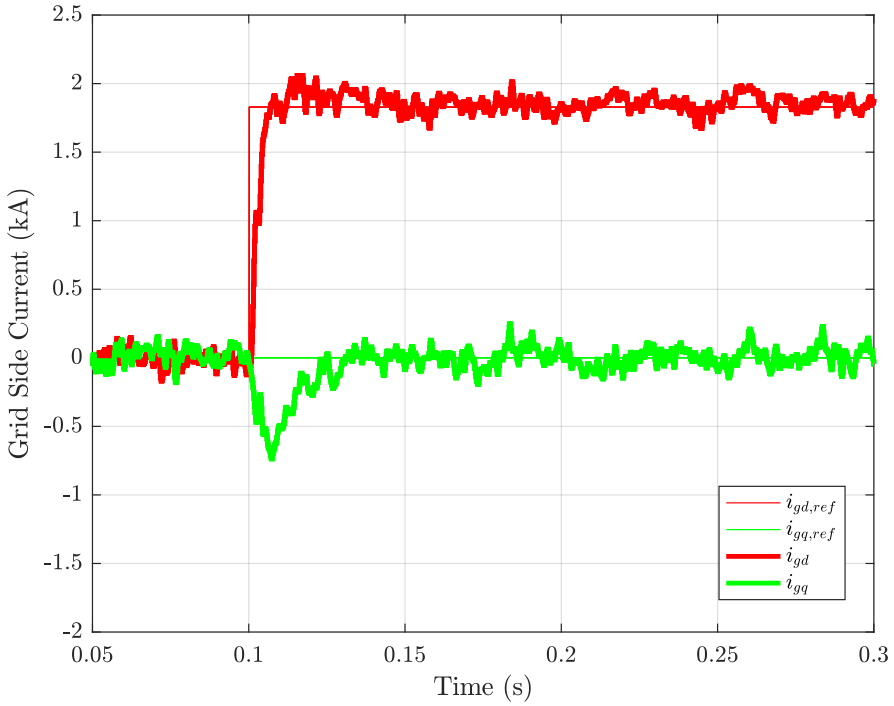

Figure 6.9: Simulation results showing sampled values of grid current i_{gd} (red), i_{gq} (green) and their corresponding references (red and green)

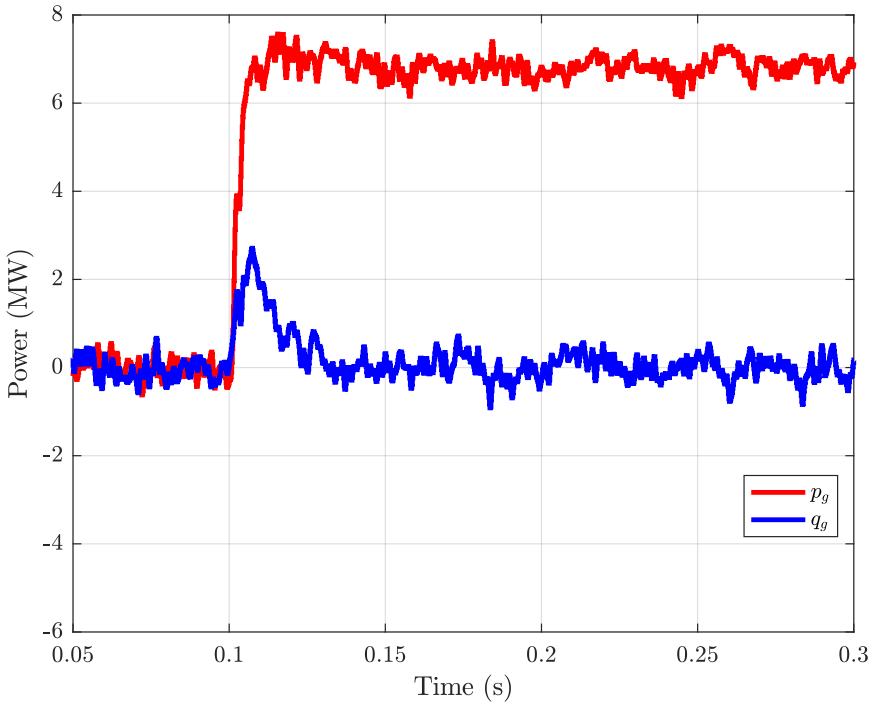

Figure 6.10: Simulation results showing sampled values of real power p_g (red) and reactive power q_g (blue) at the point of common coupling (PCC).

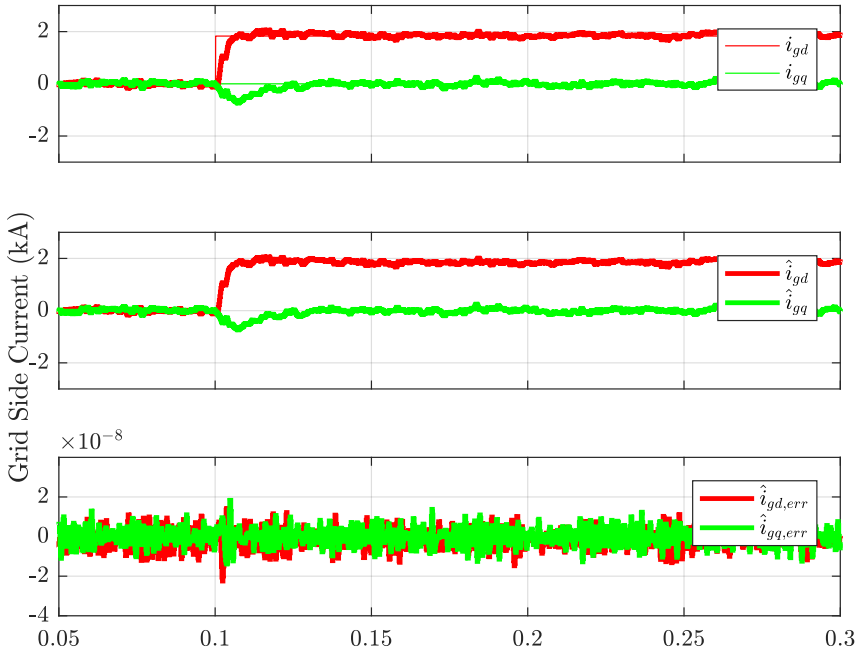

Figure 6.11: Simulation results showing sampled values of the augmented observer: Measured grid current $\boldsymbol{i}_{\mathrm{g}}$, estimated grid current $\hat{\boldsymbol{i}}_{\mathrm{g}}$ and error between measured and estimated grid current in dq coordinates.

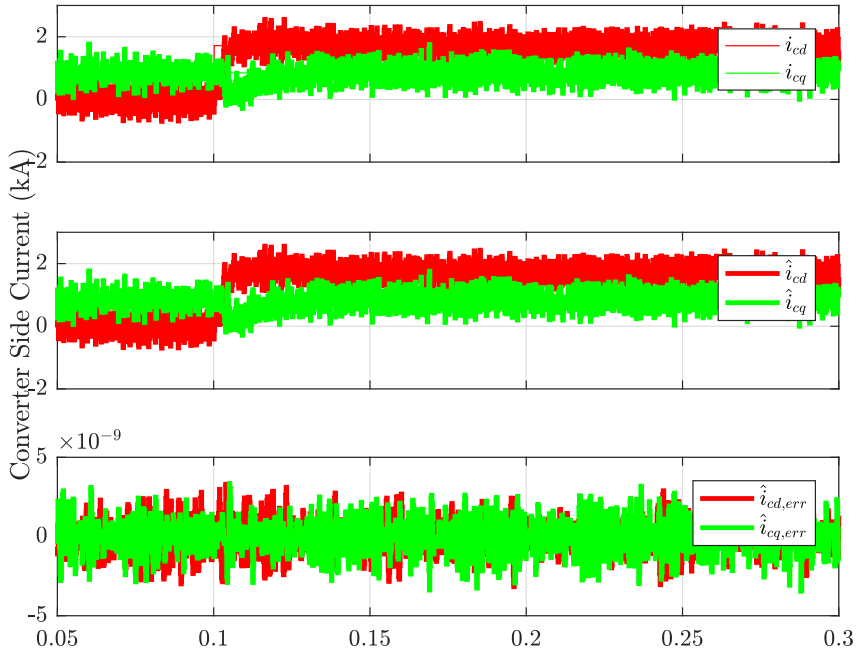

Figure 6.12: Simulation results showing sampled values of the augmented observer: Measured converter current $\boldsymbol{i}_{\mathrm{c}}$, estimated converter current $\hat{\boldsymbol{i}}_{\mathrm{c}}$ and error between measured and estimated converter current in dq coordinates.

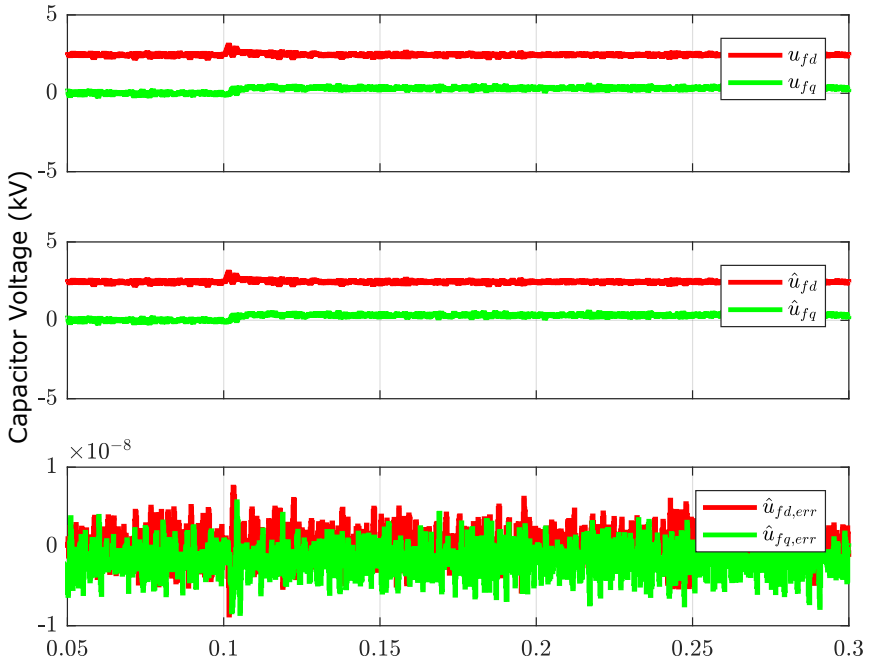

Figure 6.13: Simulation results showing sampled values of the augmented observer: Measured capacitor voltage $\boldsymbol{u}_{\mathrm{f}}$ in kV, estimated capacitor voltage $\hat{\boldsymbol{u}}_{\mathrm{f}}$ in kV and error between measured and estimated capacitor voltage in dq coordinates.

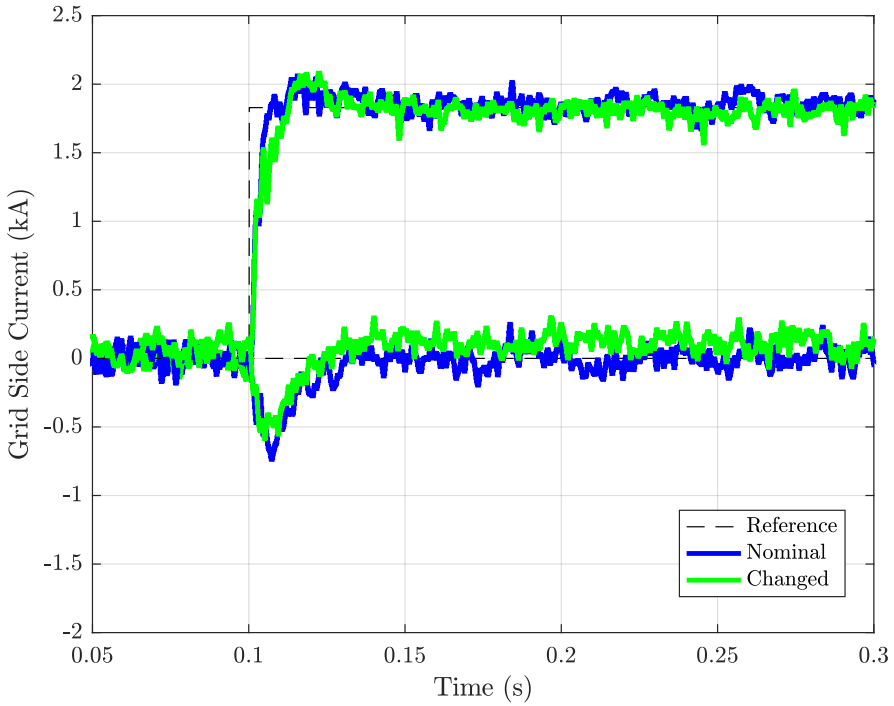

Figure 6.14: Simulation results showing sampled values of i_g (blue) with nominal filter parameters, i_g (green) with filter parameters increased by 10 % and reference current (black) .

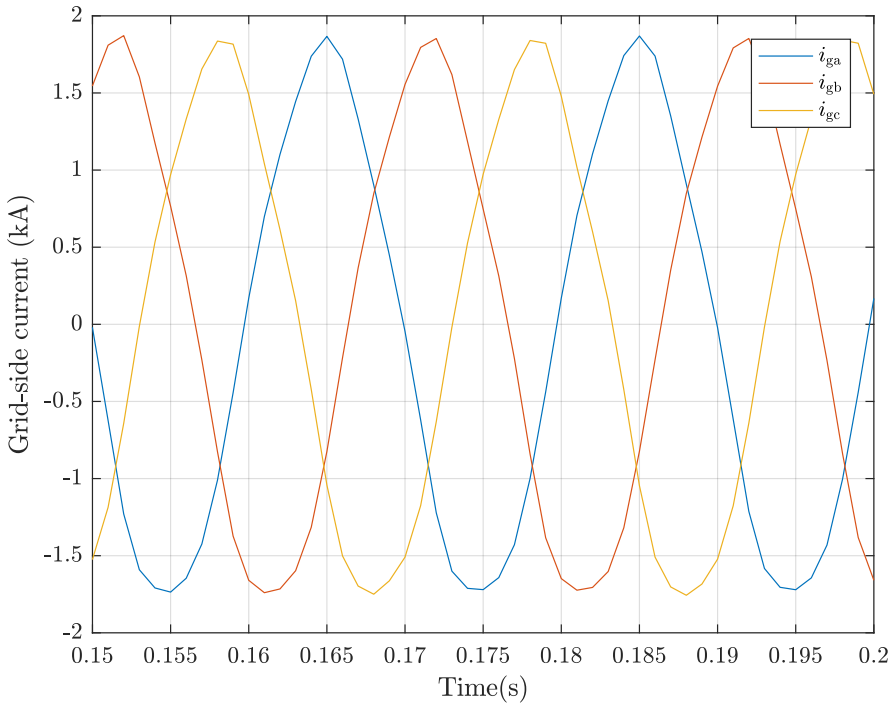

Figure 6.15: Three-phase grid current simulated using state-space controller based upon filter parameters given in Table 6.1.

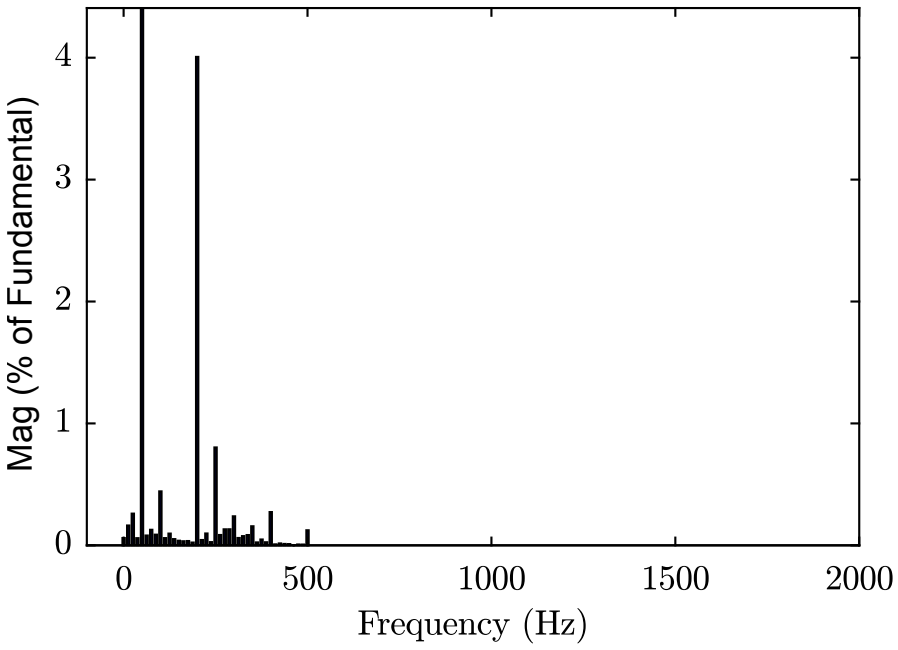

Figure 6.16: Grid-side current spectrum simulated using state-space controller based upon filter parameters given in Table 6.1: THD = 4.15%, f_{sw} = 1 kHz.

7 Conclusion

In this thesis, the discrete-time model and current control of a grid converter equipped with an LCL filter based upon finite set model predictive control were studied. The exact discrete-time model of the system was studied with the ZOH assumed in the stationary coordinates, where it occurs naturally. The presented discrete-time model of the system can be applied for the design, analysis and implementation of controllers and observers. Based upon the exact discrete-time model of the system, the trajectory of converter current is predicted for future time instant to generate optimal switching state. Digital implementation requires to include the delay due to ZOH inside the controller and delay due to computational burden. Both of these delay (computational and ZOH) were included in the control algorithm.

The tracking of current reference at a switching frequency below 1 kHz and THD below 5% was achieved with a tracking error of 0.45%. The issue of resonance damping was addressed through virtual resistor active damping concept. The results show that the LCL resonance was well damped. The robustness of the controller against parameter variation was analyzed. The simulation results show that the system remains stable against a parameter error of 10%. An observer was designed to estimate the state and reduce the number of sensors required to run the controller. The results show that the observer can estimate the state elements with high accuracy and these estimates can be used to run the controller successfully.

The computational burden of FS model predictive control algorithm is high even for a prediction horizon of one and the computational burden increases exponentially with the increase in prediction horizon. This makes the real-time implementation of the control algorithm very challenging for LCL filters designed for low voltage application.

The performance of FS model predictive current controller was compared to the performance of observer based state-space controller at low switching frequency (below 1 kHz) suitable for medium voltage application. The results show that the performance of FS model predictive current controller was better than observer based state-space controller in terms of achieving better THD at low switching frequency.

A suitable topic for future research is to improve the current tracking by decoupling the d & q axis. Next-stage would be to include grid harmonic attenuation and grid voltage estimation to enhance the overall performance of the controller. A method to reduce the steady-state error at low switching frequency while maintaining THD within grid standard can be devised.

References

[1] J. Kukkola, M. Hinkkanen, and K. Zenger, "Observer-based state-space current controller for a grid converter equipped with an lcl filter: Analytical method for direct discrete-time design," *IEEE Transactions on Industry Applications*, vol. 51, no. 5, pp. 4079–4090, Sept 2015.

[2] N. Panten, N. Hoffmann, and F. W. Fuchs, "Finite control set model predictive current control for grid-connected voltage-source converters with lcl filters: A study based on different state feedbacks," *IEEE Transactions on Power Electronics*, vol. 31, no. 7, pp. 5189–5200, July 2016.

[3] H. Miranda, R. Teodorescu, P. Rodriguez, and L. Helle, "Model predictive current control for high-power grid-connected converters with output lcl filter," in *Industrial Electronics, 2009. IECON '09. 35th Annual Conference of IEEE*, Nov 2009, pp. 633–638.

[4] P. A. Dahono, "A control method to damp oscillation in the input lc filter," in *Power Electronics Specialists Conference, 2002. pesc 02. 2002 IEEE 33rd Annual*, vol. 4, 2002, pp. 1630–1635.

[5] S. Kouro, M. A. Perez, J. Rodriguez, A. M. Llor, and H. A. Young, "Model predictive control: Mpc's role in the evolution of power electronics," *IEEE Industrial Electronics Magazine*, vol. 9, no. 4, pp. 8–21, Dec 2015.

[6] J. Rodriguez and P. Cortes, *Predictive Control of Power Converters and Electrical Drives*, 1st ed. Wiley-IEEE Press, 4 2012. [Online]. Available: http://amazon.com/o/ASIN/1119963982/

[7] H. A. Young, M. A. Perez, J. Rodriguez, and H. Abu-Rub, "Assessing finite-control-set model predictive control: A comparison with a linear current controller in two-level voltage source inverters," *IEEE Industrial Electronics Magazine*, vol. 8, no. 1, pp. 44–52, March 2014.

[8] C. Bordons and C. Montero, "Basic principles of mpc for power converters: Bridging the gap between theory and practice," *IEEE Industrial Electronics Magazine*, vol. 9, no. 3, pp. 31–43, Sept 2015.

[9] P. Cortes, J. Rodriguez, D. Quevedo, and C. Silva, "Predictive current control strategy with imposed load current spectrum," in *Power Electronics and Motion Control Conference, 2006. EPE-PEMC 2006. 12th International*, Aug 2006, pp. 252–257.

[10] A. R. J. Geldenhuys, H. Mounton and T. Geyer, "Model predicitve control of a grid connected converter with lcl filter," *ABB corporate research*, Oct 2016.

[11] "Ieee recommended practice and requirements for harmonic control in electric power systems - redline," *IEEE Std 519-2014 (Revision of IEEE Std 519-1992) - Redline*, pp. 1–213, June 2014.

[12] S. Mariethoz and M. Morari, "Explicit model-predictive control of a pwm inverter with an lcl filter," *IEEE Transactions on Industrial Electronics*, vol. 56, no. 2, pp. 389–399, Feb 2009.

[13] R. Teodorescu, M. Liserre, and P. Rodriguez, *Grid Converters for Photovoltaic and Wind Power Systems*, 1st ed. Wiley, 2 2011.

[14] J. Rodriguez, P. Cortes, R. Kennel, and M. P. Kazrnierkowski, "Model predictive control – a simple and powerful method to control power converters," in *Power Electronics and Motion Control Conference, 2009. IPEMC '09. IEEE 6th International*, May 2009, pp. 41–49.

[15] P. Cortes, J. Rodriguez, C. Silva, and A. Flores, "Delay compensation in model predictive current control of a three-phase inverter," *IEEE Transactions on Industrial Electronics*, vol. 59, no. 2, pp. 1323–1325, Feb 2012.

[16] T. Geyer, *Model Predictive Control of High Power Converters and Industrial Drives*, 1st ed. Wiley, 11 2016.

[17] J. Kukkola and M. Hinkkanen, "Observer-based state-space current control for a three-phase grid-connected converter equipped with an lcl filter," *IEEE Transactions on Industry Applications*, vol. 50, no. 4, pp. 2700–2709, July 2014.

[18] Z. Song, C. Xia, and T. Liu, "Predictive current control of three-phase grid-connected converters with constant switching frequency for wind energy systems," *IEEE Transactions on Industrial Electronics*, vol. 60, no. 6, pp. 2451–2464, June 2013.

[19] J. Scoltock, T. Geyer, and U. K. Madawala, "A model predictive direct current control strategy with predictive references for mv grid-connected converters with lcl -filters," *IEEE Transactions on Power Electronics*, vol. 30, no. 10, pp. 5926–5937, Oct 2015.

[20] T. Geyer, "Computationally efficient model predictive direct torque control," *IEEE Transactions on Power Electronics*, vol. 26, no. 10, pp. 2804–2816, Oct 2011.

[21] G. Prior and M. Krstic, "A control lyapunov approach to finite control set model predictive control for permanent magnet synchronous motors," *Journal of Dynamic Systems, Measurement and Control*, vol. 137, Jan 2015.

[22] L. Wang, S. Chai, D. Yoo, L. Gan, and K. Ng, *PID and Predictive Control of Electrical Drives and Power Converters using MATLAB / Simulink*, 1st ed. Wiley-IEEE Press, 3 2015.

[23] T. Geyer and D. E. Quevedo, "Multistep finite control set model predictive control for power electronics," *IEEE Transactions on Power Electronics*, vol. 29, no. 12, pp. 6836–6846, Dec 2014.

[24] J. Scoltock, T. Geyer, and U. K. Madawala, "A model predictive direct current control strategy with predictive references for mv grid-connected converters

with lcl -filters," *IEEE Transactions on Power Electronics*, vol. 30, no. 10, pp. 5926–5937, Oct 2015.

[25] G. F. Franklin, J. D. Powell, and M. L. Workman, *Digital Control of Dynamic Systems (3rd Edition)*, 3rd ed. Addison-Wesley, 12 1997.

Appendix A

The elements of the system matrix $\mathbf{\Phi}, \mathbf{\Gamma}_{\mathrm{c}}$ and $\mathbf{\Gamma}_{\mathrm{g}}$ are as follows

$$\mathbf{\Phi} = \mathrm{e}^{\mathbf{A}T_s} = \begin{bmatrix} a_{11} & a_{12} & a_{13} \\ a_{21} & a_{22} & a_{23} \\ a_{31} & a_{32} & a_{33} \end{bmatrix} = \boldsymbol{P} e^{\wedge T_s} \boldsymbol{P}^{-1} \tag{7.1}$$

The closed form solution for the element is calculated using eigen decomposition $\mathbf{A} = \boldsymbol{P} \wedge \boldsymbol{P}^{-1}$. The eigen value $(\wedge)$ and eigen vector $(\mathbf{P})$ matrices are

$$\boldsymbol{P} = \begin{bmatrix} -\frac{L_{fg}}{L_{fc}} & 1 & -\frac{L_{fg}}{L_{fc}} \\ -j\omega_p L_{fg} & 0 & j\omega_p L_{fg} \\ 1 & 1 & 1 \end{bmatrix}; \ \wedge = \begin{bmatrix} -j(\omega_g + \omega_p) & 0 & 0 \\ 0 & -j\omega_g & 0 \\ 0 & 0 & -j(\omega_g + \omega_p) \end{bmatrix} \tag{7.2}$$

With this decomposition matrix the exponential can be calculated element wise. The resultant matrix is

$$\mathbf{\Phi} = \boldsymbol{\gamma} \begin{bmatrix} \frac{L_{fc} + L_{fg} cos(\omega_p T_s)}{L_t} & -\frac{sin(\omega_p T_s)}{\omega_p L_{fc}} & \frac{L_{fg}[1 - cos(\omega_p T_s)]}{L_t} \\ \frac{sin(\omega_p T_s)}{\omega_p C_f} & cos(\omega_p C_f) & -\frac{sin(\omega_p T_s)}{\omega_p C_f} \\ \frac{L_{fc}[1 - cos(\omega_p T_s)]}{L_t} & \frac{sin(\omega_p T_s)}{\omega_p L_{fg}} & \frac{L_{fg} + L_{fc} cos(\omega_p T_s)}{L_t} \end{bmatrix} \tag{7.3}$$

where $\boldsymbol{\gamma} = e^{-j\omega_g T_s}$, and $L_t = L_{fc} + L_{fg}$.

The system matrix $\mathbf{\Gamma}_{\mathrm{c}}$ for converter voltage $\boldsymbol{u}_{\mathrm{c}}$ is

$$\mathbf{\Gamma}_{\mathrm{c}} = \left(\int_0^{T_s} \mathrm{e}^{\wedge \tau} \mathrm{e}^{-j\omega_g (T_s - \tau)} d\tau \right) B_c = \begin{bmatrix} b_{c1} \\ b_{c3} \\ b_{c3} \end{bmatrix} = \boldsymbol{\gamma} \begin{bmatrix} \frac{T_s}{L_t} + \frac{L_{fg} sin(\omega_p T_s)}{\omega_p L_{fc} L_t} \\ \frac{L_{fg}[1 - cos(\omega_p T_s)]}{L_t} \\ \frac{T_s}{L_t} - \frac{sin(\omega_p T_s)}{\omega_p L_t} \end{bmatrix} \tag{7.4}$$

The system matrix $\mathbf{\Gamma}_{\mathrm{g}}$ for grid voltage $\boldsymbol{u}_{\mathrm{g}}$ is

$$\mathbf{\Gamma}_{\mathrm{g}} = \begin{bmatrix} b_{g1} \\ b_{g2} \\ b_{g3} \end{bmatrix} = \begin{bmatrix} \frac{\boldsymbol{\gamma}[-\omega_g \omega_p sin(\omega_p T_s) + j\omega_g^2 cos(\omega_p T_s) - j\delta] - j\omega_p^2}{\delta \omega_g (L_{fc} + L_{fg})} \\ \frac{\boldsymbol{\gamma}[\omega_p cos(\omega_p T_s) + j\omega_g sin(\omega_p T_s)] - \omega_p}{\delta \omega_p C_f L_{fg}} \\ \boldsymbol{\gamma} \frac{\omega_g \omega_p L_{fc} sin(\omega_p T_s) - j\delta L_{fg} - j\omega_g^2 L_{fc} cos(\omega_p T_s)}{\delta \omega_g L_{fg} (L_{fc} + L_{fg})} + \frac{j\delta L_{fg} + j\omega_g^2 L_{fc}}{\delta \omega_g L_{fg} (L_{fc} + L_{fg})} \end{bmatrix} \tag{7.5}$$

where $\delta = \omega_g^2 - \omega_p^2$.

Appendix B

The cost function J (3.13) can be written in quadratic form

$$\begin{aligned} J &= [\mathbf{F}_{dq}(k) - \Upsilon \mathbf{U}_{\mathrm{c}}(k)]^{\mathrm{T}}[\mathbf{F}_{dq}(k) - \Upsilon \mathbf{U}_{\mathrm{c}}(k)] \\ &= [\mathbf{F}_{dq}(k)]^{\mathrm{T}}[\mathbf{F}_{dq}(k)] - 2[\mathbf{U}_{\mathrm{c}}(k)]^{\mathrm{T}}\Upsilon^{\mathrm{T}}[\mathbf{F}_{dq}(k)] + [\mathbf{U}_{\mathrm{c}}(k)]^{\mathrm{T}}\Upsilon^{\mathrm{T}}\Upsilon[\mathbf{U}_{\mathrm{c}}(k)] \end{aligned}$$

The cost function J is minimized to find the optimal control.

$$\begin{aligned} \frac{\partial J}{\partial \mathbf{U}_{\mathrm{c}}} &= 0 - 2\Upsilon^{\mathrm{T}}[\mathbf{F}_{dq}] + 2\Upsilon^{\mathrm{T}}\ \Upsilon \mathbf{U}_{\mathrm{c}}(k) \\ \frac{\partial J}{\partial \mathbf{U}_{\mathrm{c}}} &= 0 \\ \Rightarrow \mathbf{U}_{\mathrm{c}}(k) &= (\Upsilon^{\mathrm{T}}\Upsilon)^{-1}\Upsilon^{T}[\mathbf{F}_{dq}] \\ \Rightarrow \mathbf{U}_{\mathrm{c}}(k) &= \Upsilon^{-1}[\mathbf{F}_{dq}] \end{aligned} \tag{7.6}$$

The unconstrained optimal control $\mathbf{U}_{\mathrm{c,unc}}$ can be obtained by combining equation (3.12) and (7.6).

$$\mathbf{U}_{\mathrm{c,unc}}(k) = \Upsilon^{-1}(\mathbf{Y}_{\mathrm{ref}}(k) - \mathbf{\Gamma x}(k) - \mathbf{\Psi U}_{\mathrm{g}}(k)) \tag{7.7}$$